Experimental crystallization of the Beauvoir granite as a model for the evolution of Variscan rare metal magmas

Michel Pichavant

To cite this version:

Michel Pichavant. Experimental crystallization of the Beauvoir granite as a model for the evolution of Variscan rare metal magmas. Journal of Petrology, 2022, 63 (12), pp.egac120. 10.1093/petrology/egac120 . insu-03851013

HAL Id: insu-03851013
https://insu.hal.science/insu-03851013v1

OXFORD UNIVERSITY PRESS | Journal of Petrology

Experimental crystallization of the Beauvoir granite as a model for the evolution of Variscan rare metal magmas

Journal:	*Journal of Petrology*
Manuscript ID	JPET-Aug-22-0134.R1
Manuscript Type:	Original Manuscript
Date Submitted by the Author:	02-Nov-2022
Complete List of Authors:	PICHAVANT, Michel; Université d'Orléans, Institut des Sciences de la Terre d'Orléans (ISTO), UMR 7327
Keyword:	experimental petrology, granite, trace element
Journal of Petrology now offers Virtual Collections of published papers. You may choose up to three collections from the list below. Virtual collections will increase the visibility of your work.:	Experimental Petrology, Ore Deposits Formation < Process Themes, Granitoids < Material Themes

Experimental crystallization of the Beauvoir granite as a model for the evolution of Variscan rare metal magmas

Michel Pichavant*

Université d'Orléans, Institut des Sciences de la Terre d'Orléans (ISTO), UMR 7327, 1A rue de la Férollerie, CS 20066, 45071, Orléans Cedex 02, France

*Corresponding author. E-mail: michel.pichavant@cnrs-orleans.fr

ABSTRACT

New experiments on the strongly peraluminous, Li-, P- and F-rich Beauvoir granite (Massif Central, France) provide a basis for understanding crystallization and chemical fractionation in Variscan rare metal magmas. Crystallization experiments were performed on two natural granite compositions under H_2O-saturated conditions at 100, 200 and 300 MPa, from 540°C to 700°C and between ~NNO+3 and NNO-1.4. Experimental charges were examined by SEM and their products (glasses and crystals) analyzed for major elements by EMPA. Trace element concentrations in selected glasses were also determined by LA ICP-MS. Despite experimental durations commonly exceeding 1000 h and some up to 4000 h, kinetic problems were encountered in particular in the 100 MPa charges whereas, at 200 and 300 MPa, results consistent with previous melting experiments were obtained. Beauvoir melts crystallize quartz, plagioclase, K-feldspar and mica as major phases. At NNO-1.4, mica is a biotite whereas it is a Li-mica between ~NNO+3 and NNO-1. Apatite, Fe-Ti oxides, either hematite or magnetite, topaz, amblygonite, cassiterite and columbite-tantalite appear as accessory phases between ~NNO+3 and NNO+1. Experimental plagioclases are albitic (An < 4.5 mol%) and more Ca and K-rich than natural albites in the granite whereas experimental K-feldspars are more sodic (Ab < 45 mol%) than the natural crystals. The less evolved starting melt crystallized Li phengites whereas the most evolved yielded Li-, F-rich micas near the polylithionite-zinnwaldite series, similar to natural micas in the granite. Equilibrium crystallization increases A/CNK, F and P and concentrates Li, Be, B, Rb, Cs, W, U in the melt. Nb and Ta are also enriched, their behavior being controlled by the solubility of columbite-tantalite in the melt. Other elements are either unchanged (Mn, Zn, Ti) or depleted (Sr, Pb) during magmatic fractionation. Sn is concentrated in Li-mica and hematite and it behaves compatibly at high fO_2. Beauvoir melts crystallize at very low temperatures, below 670°C for the two compositions studied and solidus temperatures, determined from previous melting experiments and confirmed by the new crystallization experiments, are near 550°C. The experiments demonstrate that most of the mineralogical and geochemical characteristics that make the Beauvoir granite distinctive result from magmatic rather than hydrothermal post-magmatic processes. Albitic plagioclase, Li-mica, topaz and amblygonite are of magmatic origin. Glass major element compositions suggest that the two granite samples represent crystallized liquids. Trace element fractionations for most elements at Beauvoir can be accounted for by magmatic crystallization-differentiation processes. Implications for the mineralogy, fO_2, volatile concentrations, crystallization and conditions of emplacement, fractionation mechanisms and origin of the Beauvoir granite are discussed.

Key words: rare metal granite, crystallization experiments, mica compositions, magmatic fractionation

INTRODUCTION

The Beauvoir granite (northwest French Massif Central, FMC) is a composite granitic intrusion with mineralogical and geochemical characteristics emblematic of Variscan rare metal granites (Linnen and Cuney, 2005; Breiter, 2012; Romer and Pichavant, 2021). Since Aubert (1969), the Beauvoir granite has been extensively studied. Scientific results obtained from the ~900 m long continuous core drilling Géologie Profonde de la France (GPF) program have led to an integrated petrological, geochemical, geophysical, structural and geochronological description of the Beauvoir granite and its country rocks (Cuney and Autran, 1987). This has formed the basis for metallogenic models of mineralizations associated with peraluminous granites (Cuney et al., 1992; Raimbault et al., 1995). Recently, the Beauvoir granite has attracted a renewed interest, mainly centered on the magmatic-hydrothermal evolution and on W deposition processes. Harlaux et al. (2018) have re-investigated the primary fluid inclusions hosted in quartz and topaz from the granite and the associated La Bosse W-bearing stockwork. Several episodes of wolframite generation and W deposition have been recognized in the Echassières district around the Beauvoir granite (Monnier et al., 2019; 2020).

Although the Beauvoir granite can be locally extensively transformed as a result of greisenisation and kaolinization, results from the GPF program have emphasized the magmatic evolution of the granite (Cuney and Autran, 1987). Raimbault et al. (1995) showed that the Beauvoir granite was built as several independent magma batches. Its P- and Ta-rich nature was recognized and also the geochemical similarity between the Beauvoir granite and other enriched crustal magmas such as rare element pegmatites (Raimbault et al., 1995; Cerny et al., 2005a). Subsequently, the Beauvoir granite has served as a reference for the mineralogical and geochemical characteristics of other rare metal granites such as Montebras (Marcoux et al., 2021), Argemela (Michaud and Pichavant, 2020) and Podlesi (Breiter et al., 1997) in the Variscan belt and also Pitinga (Costi et al., 2009) and Yichun (Pollard, 2021) outside the Variscan belt.

The Beauvoir granite is specific in many aspects, one of the most unusual being the very low solidus temperatures, < 600°C for H_2O-saturated conditions between 100 and 300 MPa (Pichavant et al., 1987a), i.e. more than 100°C lower than the solidus of the haplogranite Qz-Ab-Or system (Tuttle and Bowen, 1958). These low solidus temperatures have been an important anchoring point in models proposed for the origin, magmatic evolution and magmatic-hydrothermal transition of the Beauvoir granite (Aïssa et al., 1987; Cuney and Autran, 1987; Cuney et al., 1992; Fouillac and Rossi, 1991; Raimbault et al., 1995). The solidus temperature determinations were based on melting experiments and only a few crystallization experiments were performed (Pichavant et al., 1987a). Since 1987, additional experimental investigations have been carried out on the Beauvoir granite (Lahlafi, 1997; Pichavant et al., 2016; unpublished) and new constraints have become available on the magmatic evolution. The aim of this paper is to present a synthesis of experiments available on the Beauvoir granite.

Pichavant et al. (1987a) pointed out the restricted number of experimental phase equilibria available on natural rare metal granites in comparison with data on equivalent synthetic compositions. Since that time and the works of Kovalenko (1979) on ongonites and of Weidner and Martin (1987) on the Slip leucogranite from the St Austell pluton, several experimental studies have come out on highly evolved granites. Solidus and liquidus temperatures, crystallization sequences and melt fractionation trends have been determined on one sample from the vertically zoned, F-bearing Xianghualing pluton in south China (Xiong et al., 2002). Lukkari and Holtz (2007) worked out the phase relations and mutual stabilities of F-bearing phases for the Kymi topaz granite in south Finland. Aksyuk et al. (2016) presented solidus data for a biotite and a Li-F granite from the Voznesenka area, far-east Russia. More recently, phase equilibria have been determined for the different facies of the Qitianling pluton, south China (Huang et al., 2021). All these experimentally investigated granites have in common to be F-bearing or F-rich and metaluminous to slightly peraluminous and to present A-type affinities. In contrast, rare metal granites in the Variscan belt are mostly strongly peraluminous and P-rich, besides being also high in F and Li (Raimbault et al., 1995; Linnen and Cuney, 2005). This underlines the importance of phase equilibrium data on the Beauvoir granite which, together with the Slip leucogranite (Weidner and Martin, 1987), represents the only experimentally investigated example of peraluminous, P-rich natural rare metal granite composition (PHP type of Linnen and Cuney, 2005). Below, the experimental phase relations for two facies of the Beauvoir granite are presented, focusing on liquidus and solidus temperatures, crystallization sequence, melt and mineral composition trends and rare element enrichment mechanisms. The experimental results constrain the conditions of crystallization of PHP rare metal magmas in the Variscan belt (Linnen and Cuney, 2005; Roda Robles et al., 2018; Michaud and Pichavant, 2020) and provide insight on the behavior of rare metals at the magmatic stage.

THE BEAUVOIR GRANITE

The Beauvoir granite is located within the Echassières granitic complex in the northwest part of the FMC which belongs to the northern margin of Gondwana, the southern continent involved in the Variscan collision (Faure et al., 2009). The Echassières granitic complex outcrops in a tectonic window that exposes the Para-Autochtonous and Lower Gneiss Units, structurally the deepest formations of the stack of metamorphic nappes in the FMC (Faure et al., 2009). Granitic rocks from the Echassières complex, including the Colettes and the Beauvoir granite, intrude biotite-muscovite micaschists from the Para-Autochtonous Unit (Cuney and Autran, 1987; see map in Harlaux et al., 2017).

The main granite unit in the Echassières complex is the Colettes granite (surface extension 40 km^2), which is a biotite-muscovite granite. The Beauvoir granite forms a small (surface extension 0.1 km^2) satellite intrusion south of the Colettes. Field relations and previous works demonstrate that the Beauvoir is intrusive into the Colettes granite. However, radiometric ages for the two granites overlap, from 312 +/- 8 Ma (Colettes) to between 308 and 317 Ma (Beauvoir, see details in Cuney and Marignac, 2015 and Monnier et al., 2019). Both granites crosscut the quartz-wolframite veins of the La Bosse stockwork hosted in country rock micaschists south of the granitic complex. This early mineralizing episode (335 Ma, Harlaux et al., 2018; Monnier et al., 2019) has been interpreted to be genetically related to the La Bosse granite whose existence is postulated at depth (Aubert, 1969; Cuney et al., 1992; Harlaux et al., 2017).

The Beauvoir granite is mineralogically and geochemically highly specific. The GPF drill hole intersected both the upper and lower contacts of the granite with metamorphic country rocks at depths of 100 and 880 m respectively below the surface. Petrographic and structural studies show that the granite was emplaced as an inclined sheet-like body in country rock micaschists, remnants of which occur as roof pendants of several m in the upper part and as sheets at the base of the granite. Analysis of the drill core revealed that the granite is composite and consists of 3 main units (Cuney and Autran, 1987; Cuney et al., 1992), including from top to bottom the B1 (from 100 to 450 m depth), B2 (from 450 to 750 m depth) and B3 (from 750 to 880 m depth) units. Several porphyritic microgranites are encountered near the bottom of the drill hole.

Mineralogically, the Beauvoir is an albite-lepidolite granite. There are minor but systematic variations in textures and proportions of the main mineral phases (albite, lepidolite, quartz, K-feldspar) between the different facies (Rossi et al., 1987; Cuney et al., 1992; Harlaux et al., 2017). The B1 facies is hololeucocratic, rich in albite and lepidolite and relatively poor in K-feldspar and it contains globular quartz with a snowball texture. The B2 facies, slightly darker than the B1, is enriched in K-feldspar and depleted in albite and lepidolite. The B3 facies is characterized by pink perthitic K-feldspars which are more abundant than micas. The granite hosts accessory phases such as topaz, apatite, amblygonite and zircon and a rare element mineral assemblage including cassiterite, columbite-tantalite (C-T), microlite and uraninite (Rossi et al., 1987; Cuney et al., 1992).

Geochemically, the Beauvoir granite is moderately silicic (68-72 wt% SiO_2), strongly peraluminous (A/CNK = 1.25-1.45), enriched in Na (up to ~5 wt% Na_2O), P (from 1 to > 2 wt% P_2O_5) and F (from 1.5 to > 2.5 wt%) and depleted in Fe (< 0.5 wt% Fe_2O_3), Ca (< 1 wt% CaO), Ti (< 100 ppm) and Mg (< 300 ppm, Raimbault et al., 1995). Li (from ~2000 to > 5000 ppm), Sn (up to ~1500 ppm), Nb (up to ~150 ppm), Ta (up to ~450 ppm) are strongly enriched as well as W, Cs, Rb and Be whereas Ba, Pb, La, Zr, REE and Th are depleted (Raimbault et al., 1995). Fe/Mn, Nb/Ta and Zr/Hf are particularly low whereas Fe/Mg is particularly high. These enrichment and depletion patterns become progressively more marked from base to top, i.e., from the B3, B2 to the B1 unit. However, some levels within the B2 and B3 (the B' facies) preserve whole-rock compositions outside the main trends and which have been interpreted as witnesses of a magma batch less evolved than the one at the origin of the B1, B2 and B3 units (Raimbault et al., 1995).

The top part of the Beauvoir granite has been hydrothermally altered. Greisenisation develops along fissures and fractures and the granite transforms into a quartz-muscovite assemblage which can cover an important surface in outcrop (15 vol% in the kaolin open pit, Cuney et al., 1992). Both the Beauvoir and the Colettes granites experienced extensive kaolinization. However, hydrothermal alteration is generally inconspicuous in core samples (Cuney et al., 1992) and of negligible importance from a geochemical point of view, except for Sr and Be concentrated in late phosphate minerals (Raimbault et al., 1995; Charoy et al., 2003). Yet, this does not necessarily ensure that granite whole-rocks are equivalent to magma compositions since some elements (in particular F and Li) are enriched in micaschists around the granite. These elements were probably extracted by late-magmatic fluids coming from the Beauvoir magma (Cuney et al., 1992).

EXPERIMENTAL METHODS

Starting materials

Two Beauvoir granite samples were selected from the GPF drill core, one from the B1 (depth: 278.20-279.95 m) and the other from the B2 (depth: 606.05-606.95 m) unit. Both samples were crushed and sieved to grain sizes of ~50 µm. The resulting rock powders were analysed for major elements plus FeO, F, CO_2, total H_2O and Li at CRPG, Vandoeuvre les Nancy (Pichavant et al., 1987a). Systematic differences consistent with those noted at the scale of the entire GPF core appear between the two samples. The B1 is more sodic and peraluminous, less potassic and so more evolved than the B2. Total Fe concentrations decrease from the B2 to the B1 sample which is also the most P-, F- and Li-rich (Table 1). Pichavant et al. (1987a) noted that the modal proportions of major phases in the two facies are in the ranges expected; both quartz and K-feldspar increase and albite and lepidolite decrease from the B1 to the B2 sample. No marked change in the major element composition of major phases was found except for lepidolite, higher in Si and F and lower in Fe in the B1 than in the B2 (Pichavant et al., 1987a).

The two rock powders were used directly in the melting experiments (Pichavant et al., 1987a). For the crystallization experiments detailed in this study, two types of starting glasses were prepared. First, hydrous glasses were synthesized by melting the two rock powders plus 5 wt% H_2O at 800°C, 100 MPa for 4 to 5 days. Second, dry glasses were prepared by melting the rock powders at 1400°C, 0.1 MPa for ~3h. In both cases, two cycles of melting, with grinding in between, were performed to improve the chemical homogeneity of the glasses (Table 1). Both types of glasses, hydrous and dry, were crushed to grain sizes of ~50 µm and used in the crystallization experiments.

Compositions of granite whole rocks and starting glasses are compared on Table 1. The correspondence is generally good although some differences are apparent for elements present in low concentrations (e.g., 0.22 vs. 0.40 wt% CaO in B1, Table 1). Minor variability is also noted between glass batches (0.62 vs. 0.40 wt% FeO_t for B2, Table 1). These discrepancies are analytical. They reflect the different methods and uncertainties associated with the analysis of whole rocks and glasses (see below) and are not due to systematic deviations between glass and whole rock compositions.

Experiments

Crystallization experiments on the Beauvoir granite were performed over a period of more than 30 years and successively in two laboratories (Nancy and Orléans).

Unbuffered (type 1) experiments

These were carried out between 1986 and 1988 in Nancy in Tuttle-type cold-seal pressure vessels working horizontally and pressurized with Ar. Temperature was measured by external type K thermocouples and permanently recorded. Each thermocouple and bomb-furnace assembly were calibrated under pressure using an internal dual thermocouple which served to precisely locate the hot spot zone and to determine the corrections to be applied to the external temperature readings. In these experiments, temperature is known to better than +/- 10°C. Pressure, measured with a Heise manometer, is known to better than +/- 2 MPa. Run durations lasted from a minimum of 672 h (28 days) around the liquidus to a maximum of 2184 h (91 days) at subliquidus temperatures.

Experimental charges consisted of 95 % (~47 mg) of hydrous glass (containing approximately 5% H_2O) plus 5 % doubly distilled demineralized water so that the total amount of H_2O present was ~10 wt%. H_2O solubilities in F-, Li-, B- and P-rich silicic melts such as the Macusani obsidians are ~8.5 wt% at 300 MPa (Holtz et al., 1993). Therefore, Beauvoir experimental charges with 10 wt% H_2O in total are considered H_2O-saturated. Charges were loaded in Au capsules (25 mm length, 2.5 mm internal diameter, thickness 0.2 mm) subsequently sealed by arc-welding. B1 and B2 capsules were placed side by side in the same bomb to allow direct comparison of the results. A total of 24 charges were produced (12 for the B1, Table 2 and 12 for the B2, Table 3) of which 14 have been reported but only partially described (Pichavant et al., 1987a). Although the fO_2 was not controlled in these experiments, the redox conditions were highly oxidizing because of an Ar pressurizing medium very poor in hydrogen. Thus, H_2 generated by H_2O dissociation inside experimental capsules became lost to the pressurizing medium, hence lowering fH_2 and increasing fO_2. In practice, this highly oxidizing environment is marked by the common presence of thin red-brick platelets of a hematite solid solution which is particularly abundant in B2 charges (see below).

Redox-buffered (type 2) experiments

These experiments were performed to investigate the influence of fO_2 on mica crystallization in evolved silicic melts (Lahlafi, 1997; Pichavant et al., 2016; Pichavant, unpublished). Most were carried out between 1994 and 1996 in Orléans in horizontal externally heated rapid-quench cold-seal hydrothermal pressure vessels (Pichavant 1987; Schmidt et al. 1995) and at 300 MPa. Total pressure was read with a Bourdon-tube manometer with an uncertainty estimated to +/- 20 bar. Temperatures were measured permanently with a type-K thermocouple located in a well drilled at the bottom of the vessel. Temperature readings, calibrated against measurements using an internal thermocouple working under pressure, are accurate to better than +/- 10°C. At the end of the experiments, the vessel was tilted vertically and capsules slided from the hot spot to the cold bottom part of the vessel in a few seconds. Different techniques were employed to control and vary the redox conditions (see Pichavant et al., 2016 for details). The *oxidizing experiments* were all performed using Ar as pressurizing gas yielding a moderately oxidizing fO_2 around NNO + 1 (ΔNNO = +1, Lahlafi, 1997; Pichavant et al., 2016). They include one experiment on the B1 (Table 2) and six on the B2 (four at 620°C and two at 700°C, both regrouped in Table 3) which have been previously partially described (Lahlafi, 1997; Pichavant et al., 2016). They lasted from 1008 h (42 days) to 4032 h (168 days). The *reducing experiments*, all on the B2 (three at 620°C regrouped in Table 3, one at 630°C and one at 700°C) have been previously partially described (Lahlafi, 1997; Pichavant et al., 2016) except the one at 630°C. Most employed the double capsule method of Eugster (1957). A Co-CoO buffer assemblage was used, yielding a ΔNNO of around – 1.4 (Table 3). The buffer was loaded into a 0.4 mm wall thickness external Au capsule to minimize H_2 loss toward the Ar gas and experimental durations were limited to 360 h (15 days). The 630°C experiment was performed in 2017 in an internally-heated pressure vessel (Scaillet et al., 1995) pressurized with an Ar-H_2 gas mixture to control the fO_2 (Table 3). Total pressure was permanently recorded and is known to better than +/- 20 bar. Temperature was continuously measured by three thermocouples with an uncertainty of +/- 5°C. The experiment lasted for 1123 h (48 days) under an experimental fO_2 of NNO-1 (ΔNNO = -1) as determined from CoPd solid sensors (Michaud et al., 2021). At the end of the experiment, the power to the furnace was switched off and temperature dropped by about 300°C during the first 4 mn. Last, one *two-stage reducing – oxidizing experiment* was performed on the B2 (Pichavant et al., 2016).

All these experiments used Au capsules as containers (inner diameter: 2.5 mm, length: 20 mm, wall thickness: 0.2 mm). Charges consisted of about 50 mg of the dry glass plus about

5 mg of doubly distilled demineralized water so that the proportion of H_2O was kept at ~10 wt.% of the total charge which, from above, corresponds to H_2O-saturated conditions.

Following quench, pressure vessels were opened. Experimental capsules were weighted to check for leaks, then opened and charges recovered to be analysed.

Analytical methods

Analysis of experimental charges focused on solid phases, glasses and crystals. No attempt was made to recover and analyze the fluid phase. Initially, Pichavant et al. (1987a) used optical microscopy and X-ray diffraction for charge characterization. Later, scanning electron microscopy (SEM) became the main phase identification tool (Lahlafi, 1997; Pichavant et al., 2016). In this study, experimental phase assemblages have been determined by SEM and optical microscopy, and confirmed from electron microprobe data and mass balance calculations. Several charges previously analysed by X-ray diffraction were examined by SEM to check the consistency of phase identification between the two methods. Most type 2 experimental charges were examined with a JEOL 6100 scanning electron microscope (BRGM, Orléans) under conditions summarized in Lahlafi (1997) and Pichavant et al. (2016). More recently, a Zeiss Merlin Compact (ISTO, Orléans) instrument operating under either secondary or back-scattered electron (BSE) mode and fitted with a Bruker energy dispersive system (EDS) was used for the type 1 and some type 2 experimental charges.

Building on the rare analyses of feldspars from crystallization experiments in Pichavant et al. (1987a), experimental charges were analysed by electron microprobe (EMPA) and the major element compositions of experimental glasses and crystals systematically determined. Most type 2 experimental charges were analysed using a CAMECA SX 50 instrument (BRGM-CNRS) working under 15 kV acceleration voltage, 12 nA sample current and 10 and 5 s counting time on peak and background respectively (Lahlafi, 1997; Pichavant et al., 2016). For the analysis of glasses, the beam was defocussed to 10 μm (vs. 1-2 μm for crystals) and the raw Na_2O and K_2O concentrations were corrected using a Macusani glass (Pichavant et al., 1987b) secondary standard following procedures detailed in Pichavant (1987). More recently, type 1 and some type 2 experimental charges were analysed using a CAMECA SX Five instrument (ISTO-BRGM) working under 15 kV acceleration voltage, 6 nA sample current and 10 and 5 s counting time on peak and background respectively. For the analysis of glasses, the beam was defocused to 10 μm and focused to 1-2 μm for crystals. Silicate analytical programs (Si, Ti, Al, Fe, Mn, Mg, Ca, Na, K with P and F) were used. In some sessions, Rb and Sn were added to the list of elements analysed but the Rb data were discarded because of an interference with Si. Sn was also analysed separately under higher sample current (20 nA) and counting times (60 and 30 s on peak and background). Attempts were made to circumvent the problem of Na_2O and K_2O migration in glass. Time series data established that alkali concentrations in experimental Beauvoir glasses strongly decrease with counting time and, for a given counting time, with the sample current. “Zero time” calculations (using number of counts calculated at t = 0 s rather than number of counts measured after t = 10 s) were tested but this resulted in small insufficient corrections. Combining results from time series measurements with analysis of secondary standards (Pichavant, 1987), correction factors from to 15 to 25% and 5 to 7.5% respectively for Na_2O and K_2O were applied to the raw glass data. For glasses, relative analytical errors, determined as standard deviations on multiple analyses on Macusani glass JV2, are: SiO_2 (0.5–1%), TiO_2 (80%), Al_2O_3 (1–1.5%), FeO (25%), MnO (100%), MgO (100%), CaO (15%), P_2O_5 (20%), F (5-10%). For Na_2O and K_2O, the relative analytical errors are estimated to 5-10%.

Micas were too small to be analysed in all charges with the electron microprobe. This difficulty was circumvented by using the EDS coupled with the Zeiss Merlin Compact SEM to estimate mica compositions. The analyses were performed with an acquisition time of 30 s and a sample current of 600 pA. The internal calibration of the instrument was used unmodified and the data were processed with the ESPRIT2.3 software from Bruker. The SEM data were compared with EMPA compositions of experimental micas analyzed in the same charge. For most elements (Si, Al, Fe, Mg, Na, K, P), relative differences between SEM and EMPA results were lower than the analytical errors of the electron microprobe. F was the only element significantly underestimated by SEM (by an average factor of 2.3) and F concentrations were corrected accordingly.

Proportions of glass and major mineral phases present in experimental charges were determined by mass balance, knowing the composition of the bulk charge (Table 1) and of each phase present from electron microprobe data. The calculations were performed on eight major oxides (SiO_2, TiO_2, Al_2O_3, FeO, MgO, CaO, Na_2O, K_2O) simultaneously (i.e., using input matrices with eight rows) and with a variable number of phases (depending on the assemblage present in the charge) using linear least square procedures detailed in Albarède (1995).

Experimental glasses and quartz crystals were analysed for trace elements by LA ICP-MS. A RESOlution -SE 193 nm excimer laser coupled to an Agilent 8900 QQQ ICP-MS was used (ISTO-IRAMAT). Ablation was performed at 10 Hz (glass) and 7 Hz (Qz) and a fluence of 4 J.cm−2. The spot diameter was set at 10 μm. SiO_2 from electron microprobe analysis was used as an internal standard, NIST610 as an external standard (Pearce et al. 1997) and Macusani glass JV2 (Pichavant et al. 1987b) as control. Reference glasses (NIST610 and Macusani) were analyzed three times at the beginning and at the end of each run of ten analyses. A total of 28 isotopes (Li7, Be9, B11, Na23, Al27, Si29, P31, K39, Ti49, Mn55, Zn66, Ge72, Rb85, Sr88, Zr90, Nb93, Sn118, Cs133, Ba137, La139, Sm147, Eu153, Gd157, Yb172, Ta181, W182, Pb208, U238) were measured. The raw data were processed off-line using the Glitter software where time-resolved signals were examined one by one. Element concentrations were calculated for the initial ~ 30 s of all ablation signals relative to the gas blank (~ 20 s), with a linear interpolation across standard analyses.

RESULTS

Experimental products and textures

Phase assemblages and proportions determined by mass balance (major phases only) are detailed in Table 2 and 3 for the B1 and B2 experiments respectively. Glass is the most abundant phase in the charges, being readily identified by optical methods and SEM. It frequently contains fluid inclusions of small to medium size (10-30 µm) homogeneously distributed in the charge. All glass-containing charges appeared as solid consolidated beads upon opening the capsule. In contrast, the B1N-16 charge (the only one without glass present, Table 2) was recovered as a soft loose powder.

Phases crystallizing from Beauvoir granitic melts include quartz (Qz), an albitic plagioclase (Pl) and K-feldspar (Af). SEM observations show that Qz forms euhedral, faceted, mostly equant and sometimes globular crystals up to 20-30 µm large (Fig. 1a) which can contain inclusions of micrometric micas. In charges close to the liquidus, Pl crystallizes as euhedral elongated laths isolated in glass, typically 10-15 µm long but which can reach ~100 µm in some B1 experiments (Fig. 1b). They appear uniformly grey and so chemically homogeneous in BSE mode (Fig. 1b). In contrast, in sub-liquidus charges, feldspars grow to sizes generally larger than under near-liquidus conditions, up to ~100 µm. Small euhedral Qz crystallize at their extremities (Fig. 1c). These large feldspars are chemically heterogeneous. They are made up of white to dark grey domains in BSE mode corresponding to K- and Na-rich zones (Fig. 1c). In some crystals, the transition from one zone to the other is progressive and geometrically complex (Fig. 1c). In others, the two zones are well separated, both geometrically and compositionally, and two chemically homogeneous feldspar phases, Pl and Af can be individualized (Fig. 1d). Af most commonly appears as small (maximum 15 µm) euhedral homogeneous K-rich phases coexisting with Pl in composite crystals (Fig. 1d) and was unfrequently found as isolated crystals isolated in glass.

Beauvoir melts have been shown previously to crystallize a mica phase (Pichavant et al., 1987a; Lahlafi, 1997; Pichavant et al., 2016). Under the most reducing conditions corresponding to the CCO buffer (NNO-1.4), biotite (Bt) is the liquidus phase at 300 MPa in B2 (experiments B2O-38/40, Table 3; Lahlafi, 1997; Pichavant et al., 2016). This Bt is a moderately F-rich siderophyllite (Pichavant et al., 2016). It amounts to several wt.% of the charge and reaches a maximum size of 30–40 μm (see Fig. 1b in Pichavant et al., 2016). For strongly oxidizing (NNO+3) to moderately reducing conditions (NNO-1) in B2 (Table 3) as well as between NNO+3 and NNO+1 in B1 (Table 2), Beauvoir melts crystallize a Li-, F-bearing mica. This mica (designated below as Li-mica, Li-Mi) has compositions ranging from relatively Li-, F-poor and mainly dioctahedral to Li-, F-rich and markedly trioctahedral. SEM observations show that Li-Mi appears mostly as platelets, either elongated as in B2 (Fig. 1e) or more rectangular and equant as in B1 charges, sometimes forming aggregates and inclusions in quartz and feldspars. Li-Mi is generally very flat and thin, typically 10-15 μm long and 2-3 μm large in B2 (Fig. 1e) and ~2 μm long and 1-2 μm large in B1 charges (Fig. 1f; g). Exceptionally, Li-Mi can be up to several tens μm long in some B2 charges (experiments B2O-2/5, Table 3, see Fig. 1a in Pichavant et al., 2016).

Several accessory phases were encountered although the accessory assemblage was not systematically determined in all charges. The most systematic include apatite (Ap) in both B1 and B2 charges and Fe-Ti oxides in B2 charges only, either hematite (Hm) or magnetite (Mt, Table 2; 3). Ap forms small subhedral crystals up to 5-10 μm (Fig. 1e), sometimes but rarely larger and often grouped in aggregates. In the type 1 experiments which are the most oxidized (NNO+3), Hm forms thin red-brown losange-shaped platelets up to several tens μm long (Fig. 1h), readily detected by optical microscopic examination and locally abundant in B2 charges (B2N-19, B2N-20, Table 3). In the less oxidized type 2 experiments (NNO+1) on B2, a small (a few μm) sub-hexagonal oxide phase identified as magnetite (Lahlafi, 1997) is present. No Fe-Ti oxide crystallized in B2 experiments performed at NNO-1 and NNO-1.4, (Table 3). Topaz was extensively looked for but only found in one charge, B1N-21, where it appears as small (< 5 μm) homogeneously distributed euhedral prisms slightly brighter than quartz and feldspar in BSE mode (Fig. 1f, g). This B1N-21 charge contains an Al-, F-rich phosphate phase of the amblygonite-montebrasite series present together with apatite. It forms relatively abundant, subhedral 10 μm large crystals darker than the other phases in BSE mode (Fig. 1g). Cassiterite and C-T are conspicuous in B1 as well as in B2 charges.

Experimental phase relations

Results of the crystallization experiments are reported in Table 2 and 3 for the B1 and B2 starting compositions respectively. Below, we focus on results in the strongly oxidizing to moderately reducing fO_2 range (from NNO+3 to NNO-1, Table 2; 3), i.e., the most reducing (NNO-1.4) B2O-38/40 and B2O-41 charges are excluded. Therefore, only conditions of crystallization of Qz, Af, Pl and Li-Mi are discussed and those for Bt are not considered further.

Some inconsistencies were found between experiments in the sense that the same P-T conditions did not always yield the same phase assemblages. For example, at fixed T and P (620°C and 300 MPa) for the B1 composition, Li-Mi is present in B1N-22 (type 1 experiment) whereas it is absent in B1O-1 (type 2 experiment) which also lacks Af and Qz (Table 2). For the B2 composition, both Pl and trace Af crystallized in B2O-2/5 (type 2 experiment) at 620°C and 300 MPa whereas these two phases are absent in B2N-25 (type 1 experiment, Table 3) performed under the same P-T conditions. These inconsistencies are attributed to several experimental factors such as use of different equipment and contrasted experimental durations. By opposite, phase identification issues are not considered responsible for these inconsistencies. Phase assemblages are identical, whether determined from SEM (this study) or X-ray diffraction (Pichavant et al., 1987a). Starting compositions were successfully mass balanced from linear combinations of phases present in the charges (low Σr^2 in Table 2 and 3), implying that our phase identification methods are reliable. In only one case (B1N-1), 2 wt% Qz (undetected by X-ray and SEM) had to be added to the phase assemblage for the charge to be successfully mass balanced. In the same way, the presence of fluid inclusions in most charges confirms that H_2O-saturated conditions (i.e., $aH_2O = 1$) were effectively imposed. Thus, differences in phase assemblages for fixed composition and P, T conditions cannot be due to aH_2O being variable between charges although, in this study, melt H_2O concentrations have not been determined. Beauvoir melt inclusions contain between 3.6 and 6.2 wt% H_2O (Kovalenko et al., 1998).

These inconsistencies have been considered in the construction of the P-T diagrams (Fig. 2; 3). For the B1, saturation curves at 300 MPa exclude two experimental charges, B1O-1 and B1N-15 (Table 2). SEM observations and mass balance calculations show that these charges are much less crystallized than the others at the same pressure (B1N-21 and B1N-22, Table 2). Moreover, Qz, Af and Li-Mi are absent in B1O-1 and B1N-15 whereas all are present in B1N-22 (Table 2). These inconsistencies are attributed to differences in experimental durations, much shorter for B1O-1 (1008 h) and B1N-15 (1104 h) than for B1N-21 and B1N-22 (2184 h, Table 2). For the B2, the Pl and Af saturation curves pass at temperatures slightly lower (-10 and -20°C respectively) than the 300 MPa B2O-2/5 type 2 charges which contain Pl and trace Af. In other words, results from the B2N-25 and B2N-24 type 1 charges (Table 3) were preferred.

For the B1 composition, the 100 MPa solidus is bracketed by the 540°C glass absent (B1N-16) and the 560°C trace glass present (B1N-11) charges. The 300 MPa solidus is half-bracketed by the 580°C glass bearing (B1N-21) charge (Table 2). Although solidus temperatures determined from melting experiments are preferred because of the possibility of supercooling problems in crystallization experiments (Pichavant et al., 1987a and see below), the latter are only ~20°C lower than the former at 100 MPa (Fig. 2). At this pressure, Qz, Pl, Af and Li-Mi all saturate from 590°C to > 600°C. Remarkably, temperatures of Qz, Pl and Af saturation are higher at 300 MPa (from 625°C to > 640°C) than at 100 MPa (Fig. 2). This is symptomatic of kinetic difficulties (melt supercooling) at 100 MPa since, under water-saturated conditions, anhydrous phases such as Qz and feldspars must saturate at progressively lower temperatures upon increasing pressure (Tuttle and Bowen, 1958; Luth, 1976). Consequently, the Qz, Pl and Af saturation curves are drawn separated in two parts, one appropriate for 100 MPa and the other for 300 MPa. By opposite, kinetic problems are negligible for Li-Mi (see below) and Li-Mi saturation is represented by a single continuous curve with a positive slope between 100 and 300 MPa (Fig. 2). Qz, Pl and Li-Mi appear all together on the B1 liquidus (at 600°C, 100 MPa and at 640°C, 300 MPa) and so their relative crystallization order cannot be specified. They are followed by Af which is the fourth and last major phase in the sequence.

For the B2 composition, the solidus is only approached (and half-bracketed) at 100 MPa by the 560°C (B2N-12) charge which contains a trace of glass and it is < 580°C at 300 MPa (Fig. 3). The 100 MPa solidus temperature is lower by 20-30°C than the one determined from the melting experiments (Pichavant et al., 1987a). Qz and Pl crystallize at progressively lower temperatures at 300 (615-625°C) than at 200 MPa (> 640°C), as expected under water-saturated conditions (Tuttle and Bowen, 1958; Luth, 1976). In comparison, these two phases saturate below 640°C at 100 MPa which indicates supercooling problems at this pressure. Therefore, the Qz and Pl saturation curves are drawn in two parts, one appropriate for 100 MPa and the other for 200 to 300 MPa (Fig. 3). As supercooling problems are less important to negligible for Af and Li-Mi (see below), saturation conditions are represented by single continuous curves between 100 and 300 MPa. One notes the contrast in slope between the Li-

Mi (positive) and the Qz, Pl and Af saturation curves (all negative, Fig. 3). Li-mica is the liquidus phase at 300 MPa being joined by Qz and Pl on the liquidus at 200 MPa. At 100 MPa, the four major phases crystallize all together on the liquidus (B2N-20 charge, Table 3). The 300 MPa experiments imply that Qz crystallizes before Pl and the 300 and 200 MPa data that Af is the fourth and last major phase in the sequence (Fig. 3).

Major element compositions

Glasses

Major element compositions of experimental glasses corrected for alkali migration are reported in Table 4. Except the few data from Lahlafi (1997) which are normalized to 100 wt%, other glass analyses are shown unnormalized. Average standard deviations for SiO_2 and Al_2O_3 are no higher than analytical errors, thus indicating that the experimental glasses are homogeneous. We note that the MnO, MgO, CaO and SnO_2 concentrations are in the same range as standard deviations and in fact often lower than detection limits. They are reported only for indicative purposes in Table 4. Experimental Beauvoir glasses are extremely felsic, being composed of essentially four oxides (Si, Al, Na, K) plus P_2O_5, F and H_2O. This is reflected in the calculated normative Qz, Ab and Or concentrations which sum to more than 90-95%. Normative An contents are between 0.2 and 0.7% for the B1 and between 0.2 and 1.4% for the B2 glasses. Normative Corundum (from 4.9 to 7% for the B1 and from 2.5 to 5.5% for the B2) and A/CNK (1.37-1.60 for the B1 and 1.20-1.44 for the B2) demonstrate that all glasses are strongly peraluminous. Near-liquidus experimental glasses (e.g., B1N-15 for B1 and B2N-26 for B2, Table 4) are not markedly more peraluminous than their corresponding starting glasses (Table 1), suggesting that the influence of alkali migration on glass analyses has been satisfactorily counteracted.

Both B1 and B2 glasses display the same compositional trends with progressive crystallization and decreasing melt fraction (*f*, Fig. 4). Normative Corundum and A/CNK both increase and residual melts become progressively more peraluminous. P_2O_5 and F concentrations (n.b., not normalized to 100% anhydrous) also increase, indicating their progressive accumulation in residual melts. The most evolved B1 melts reach ~1.70 wt% P_2O_5 and ~3.3 wt% F (for ~1.50 and ~2.3 wt% in starting materials) and the most evolved B2 melts ~1.30 wt% P_2O_5 and ~2.6 wt% F (for ~1 and ~1.7 wt% in starting materials). By opposite, normative Anorthite are much lower in experimental glasses than in starting materials but the trends (Fig. 4d) are blurred by the large uncertainty on CaO in glasses by electron microprobe because of the low concentrations involved.

The major element compositions of starting materials and experimental glasses are plotted in the Qz-Ab-Or diagram (Fig. 5). Globally, the B1 are more Ab-rich and Qz-poor than the B2 compositions. The former plot left to the H_2O-saturated haplogranite minimum liquidus temperature trend (Tuttle and Bowen, 1958) whereas the latter plot mostly on the 300 MPa minimum point (Fig. 5). Both glass groups have Qz higher than H_2O-saturated minimum liquidus temperature points at 100 MPa with added F (Manning, 1981). Compositions of several glasses (see captions to Fig. 5) and starting materials overlap as expected for charges above or near the liquidus and in fact demonstrates the internal consistency of experiments and analyses. Glasses from sub-liquidus charges do not systematically vary with the phase assemblage, being tightly grouped and little dispersed around their respective starting compositions. The 300 MPa B1 glasses (B1N-23, -22, -21) show slight variations in Ab/Or at constant Qz contents whereas the 100 MPa glasses (B1N-1, B1N-17) evolve toward distinctly higher Qz contents (Fig. 5). In the same way, the sub-liquidus B2 glass compositions have constant Qz, plotting close to the starting composition (Fig. 5). Two glasses have very high Qz contents in comparison with the other B2 compositions, B2N-3 (which come from a 100 MPa experiment) and B2O-38/40 (analysis from Lahlafi, 1997). The B2N-18 glass has Qz and Or respectively lower and higher than the other B2 compositions.

Quartz

Representative major element compositions of experimental quartz are reported in Table 5. The complete database can be found in the Supplementary Material (Table S1). In most charges, quartz is very close to pure SiO_2. The only element systematically detected with the electron microprobe is Al with Al_2O_3 concentrations between 0.07 to 0.64 wt%, on average 0.23 wt%. Phases with concentrations much richer in Al_2O_3 (2.83-3.01 wt%, Table 5) were found in one low temperature 100 MPa B1 charge (B1N-17, Table 2). SEM examinations show that these Al-rich phases are morphologically and texturally identical to Qz. They coexist with Qz having “normal” Al_2O_3 concentrations in the same charge. The high Al_2O_3 analyses do not show elevated alkali contents but are systematically associated with totals in the 97.5-98 wt% range, lower than for the other Qz (Table 5). Since Li is present at elevated concentrations in the B1 starting material (1.28 wt% Li_2O, Table 1), Li incorporation in the quartz lattice according to the coupled Si = Al + Li substitution (Breiter et al., 2014) might account for the analytical results. These peculiar compositions would thus correspond to virgilite solid solutions between quartz and spodumene of stoichiometry $Li_xAl_xSi_{3-x}O_6$ (French et al., 1978; Sirbescu et al., 2017), with x ~0.10 from our data (Table 5; S1).

Feldspars

Representative compositions of experimental feldspars are reported in Table 6 and the entire database is available in the Supplementary Material (Table S2). Feldspar compositions were determined in all feldspar-bearing charges including in some previously analysed by Pichavant et al. (1987a). Despite their small size (5 µm) in some charges, overall feldspars were correctly analysed and satisfactory structural formulae (Si+Al+P = 4.01; K+Na+Ca = 0.97 apfu on average) were obtained. Three groups of compositions are distinguished corresponding to Pl, Af and heterogeneous feldspars (Fig. 1c). All three groups contain significant P_2O_5 concentrations, higher in plagioclase (from ~0.6 to ~1.4 wt% P_2O_5) than in K-feldspar (from ~0.4 to ~1 wt% P_2O_5, Table 6). The incorporation of phosphorus in experimental feldspars from this study is consistent with the peraluminous composition and elevated P_2O_5 contents of Beauvoir melts (Simpson, 1977; London, 1992; London et al., 1999).

The three groups of compositions are plotted on the An vs. Or diagram of Fig. 6. Use of a binary instead of the more familiar ternary An-Or-Ab representation is warranted since feldspars in this study have very low An (< 5%, Table 6; S2). A minor dispersion is apparent and feldspars in the same charge can have An, Or or Ab contents that differ by 1-2 % from each other. Pl are albitic with on average ~10% Or and An from ~0.5 to ~4.5% (Fig. 6). There are slight tendencies for An to increase with temperature and Or to decrease with pressure. Pl compositions from B1 and B2 charges overlap but the least An-rich (< 1.5% An) mostly correspond to B1 and the most An-rich (An > 2.5%) to B2 charges. For comparison, natural albite from starting rocks ($Or_{0.8}Ab_{98.8}An_{0.4}$, Pichavant et al., 1987a) has An at the low end of the experimental range and Or much lower than Pl from this study (Fig. 6). Af compositions are very close to binary, most being grouped between Or_{67} and Or_{73} with An contents ~0 although some compositions extend to lower Or and An > 0. No difference appears between B1 and B2 charges (Fig. 6) but Af from 100 MPa charges have lower Or than those from 300 MPa charges. Natural K-feldspar from starting rocks ($Or_{89}Ab_{11}$, Pichavant et al., 1987a) plots outside the experimental range, being much more potassic and less sodic than Af from this study. Analyses of heterogeneous feldspars yield a group of compositions intermediate between Pl and Af.

Equilibrium between feldspar pairs coexisting in the same charge was tested by using the SOLVCALC software of Wen and Nekvasil (1994) with the feldspar solution model of Nekvasil and Burnham (1987). 14 pairs from 3 B1 and 3 B2 charges were tested. 10 returned equilibration temperatures within 2-32°C of experimental values as illustrated (Fig. 6). 4 pairs were out-of-equilibrium because of Pl compositions slightly outside the solvus. Thus, a majority of feldspar pairs in our experimental charges represent compositions equilibrated on the ternary solvus. The intermediate compositions of heterogeneous feldspars are interpreted as out-of-equilibrium compositions from inside the solvus rather than as mixtures of compositions at equilibrium on the solvus (Fig. 1c; 6).

Li-micas

Li-mica compositions were determined by EMPA in B2 charges only. In B1 charges where micas are very small, compositions were estimated by SEM. Li-Mi in charge B2N-25 were analysed both by EMPA and SEM to calibrate the SEM analyses. Li_2O contents in Li-Mi were estimated from F concentrations, using the equation [di 1] of Tischendorf et al. (1997). Results were checked against mineral separate data on Beauvoir micas (Monier et al., 1987). Equation [di 1] performs very well (relative differences between measured and expected concentrations < 5%) for very Li-rich micas (from 5 to > 7 wt% Li_2O). For less Li-rich micas, [di 1] underestimates Li_2O concentrations by 15-30%. Representative EMPA and SEM compositions of experimental Li-Mi are reported in Table 7 and the entire database can be found in Table S3. The data demonstrate a marked contrast in Li-Mi compositions between the B1 and B2 charges. In B2, Li-Mi are grouped around the Li phengite end-member (n.b., the nomenclature of Tischendorf et al., 1997 is used for consistency with the representation of mica compositions) whereas, in B1, they plot around the cryophyllite end-member and so possess a marked trioctahedral character (Fig. 7a). Combining EMPA and SEM data (Table S3), Li-Mi in B2 charges have 43.6-48.3 wt% SiO_2, 29.6-34.9 wt% Al_2O_3, 1.62-7.43 wt% FeO_t, 0.07-0.60 wt% MgO, 0-0.44 wt% MnO, 0.69-2.23 wt% Na_2O and 8.9-10.2 wt% K_2O. F ranges from 1.37 to 4.91 wt% and Li_2O from 0.60 to 3.25 wt%. SnO_2 concentrations exceed the detection limit (~400 ppm Sn under our electron microprobe operating conditions), reaching values up to ~0.3 wt% SnO_2 in the more oxidized type 1 charges. For example, in charge B2N-25, SnO_2 concentrations range from 0.14 to 0.32 wt% (Table 7; S3) and nine separate analyses (not detailed in Table S3, detection limit ~200 ppm Sn) yielded an average concentration of 0.27 +/- 0.05 wt% SnO_2. Compositions of B2 Li-Mi do not systematically change with experimental P-T conditions. Yet, FeO_t broadly decreases with decreasing melt fraction and we note that Li-Mi in the reduced type 2 B2O-50 charge have lower FeO_t (2.28-2.55 wt%) than in oxidized near-liquidus charges (4.77-5.68 wt% FeO_t in B2N-25) and Sn concentrations below detection (Table 7; S3).

In the three B1 charges analyzed, Li-Mi have 50.9-56.9 wt% SiO_2, 18.2-22.0 wt% Al_2O_3, 1.24-5.40 wt% FeO_t, 0.09-2.31 wt% MgO, 1.07-3.00 wt% Na_2O and 5.29-7.42 wt% K_2O. F ranges from 7.13 to 8.79 wt% (applying the constant x 2.3 correction factor determined on B2N-25) and Li_2O from 5.32 to 7.02 wt% with [di 1] (Table 7; S3). SiO_2, Al_2O_3, K_2O, Na_2O, F and Li_2O do not significantly vary between the three charges. However, MgO progressively decreases from B1N-23, -22 to -21 (i.e., with decreasing *f*) and Li-Mi in B1N-21 has FeO_t (1.24-2.70 wt%) lower than in B1N-22 and B1N-23 (3.41-5.40 wt%, Table 7; S3) so that the former and the two latter charges plot in separate fields (Fig. 7a). Apart from the first-order differences in SiO_2, Al_2O_3, F and Li_2O between B1 and B2 micas, MgO and Na_2O are enriched and K_2O depleted in B1 compared to B2 whereas FeO_t are similar in the two mica groups (Table 7).

Accessory phases

Representative major element compositions of accessory phases are given in Table 8. Although few analyses are available and their quality is relatively poor because of the small size of the crystals, topaz, amblygonite and apatite are all very F-rich. Atomic F/(F+OH) in topaz ranges from 0.89 to 0.99 and in amblygonite from 0.94 to 0.95. Apatite are fluor-apatites with atomic F concentrations commonly exceeding 1 atom per formula unit (Table 8). F concentrations in topaz and glass from charge B1N-21 (Table 4; 8) are consistent with the proposed distribution of F between topaz and silicic melts (Soufi, 2021). In this same charge, the distribution of F between amblygonite and melt broadly follows the experimental calibration of London et al. (2001).

Experimental hematites are very Fe-rich and Ti-poor. They have a minimum of 95% Hm (Fe_2O_3, Table 8), consistent with the high fO_2 of type 1 experiments (Table 3). Hematites contain very little MnO and MgO but significant Al_2O_3 (0.79-2.71 wt%) and SnO_2 (1.39-1.57 wt%). Separate analyses (not detailed in Table 8) yielded an average of 1.81 (+/- 0.22) wt% SnO_2 for Hm in charge B2N-25. Such high Sn concentrations in Hm are consistent with those detected in coexisting Li-Mi (see above).

Trace element compositions

Trace elements were analyzed in several highly oxidizing (~NNO+3) B2 charges and in Qz crystals from one charge and concentrations of selected elements are reported in Table 9. The charges analyzed are crystallized except one which is essentially crystal-free. Yet, examination of time-resolved ablation spectra allowed glass signals to be unambiguously identified in all charges. Multiple analyses (from 2 to 6) are available on each glass. Chemical dispersions (defined as standard deviation/mean of analyses) are mostly < 10% (Table 9), globally demonstrating homogeneous trace element distributions in the experimental glasses analyzed. In some charges and for some elements, chemical dispersions are higher (> 20%). This is the case in particular for Ba and La which have low concentrations in the analyzed glasses (~1 ppm for Ba and ~0.1 ppm for La, Table 9), not much above instrumental uncertainties. For Zr and Sn which have glass concentrations respectively of 3-4 ppm and between ~15 and ~35 ppm (Table 9), the relatively high dispersions (20-30%) in some charges could reflect glass contamination by zircon and Sn-bearing phases (cassiterite, micas and hematite). Dispersions > 10% for Ta in two charges might also be due to contamination with C-T and it is possible that hematite contamination explains some Ti dispersions > 10%. Almost all Sm, Eu, Gd and Yb concentrations were below detection and these elements are not reported in Table 9.

The evolution of trace element concentrations with progressive crystallization is illustrated on Fig. 9. Experimental melt (i.e., glass) concentrations (C) referenced to those in the initial melt (C_0, represented by the essentially crystal-free charge B2N-26) are plotted as a function of the melt fraction. For most elements, concentrations increase with decreasing *f*. Li, Be, B, Cs, U are the most strongly enriched, C/C_0 reaching averages of ~1.4 (*f* ~75%) and ~1.7 (*f* ~50%, Fig. 9). Below 25% crystallization, Li, Be, B, Cs, U concentrations follow Rayleigh fractionation for a bulk mineral/melt partition coefficient (D) of 0.01 (Fig. 9), indicating a strongly incompatible behavior. Upon further lowering *f*, rates of enrichment decrease and concentrations plot on a Rayleigh fractionation trend for a higher D (0.5), suggesting that these elements become less incompatible as *f* drops. Rb and W are also concentrated in the melt although less markedly (C/C_0 ~1.2 for *f* ~50%), most probably because both are more compatible in Li-Mi than Li, B, Cs according to the muscovite/melt partition coefficients summarized by Michaud and Pichavant (2020). We conclude that the behavior of Li, Be, B, Rb, Cs, W, U reflects their globally incompatible character during crystallization of Beauvoir melts. The D values, their variability from one element to the other and their evolution with varying *f* control the observed levels of enrichment.

Nb and Ta are also concentrated in the melt during crystallization. C/C_0 are quite high, ~1.3 for Nb and ~1.5 for Ta for *f* ~ 50% (Fig. 9), indicating preferential concentration of Ta rather than Nb. However, at the difference of the group of elements above, Nb and Ta are essential structural components of C-T [$(Fe,Mn)(Nb,Ta)_2O_6$], an accessory phase present in experimental charges. Therefore, the measured glass Nb and Ta concentrations should represent C-T solubilities provided that chemical equilibrium is established between melt and accessory phases in the experiments. C-T solubilities in silicic melts are complex functions of temperature and compositions of the melt and of the C-T phase (Linnen and Keppler, 1997; Linnen, 1998; Van Lichtervelde et al., 2018). At a temperature of 600°C appropriate for Beauvoir melts, the calculated Nb concentration of a 500 ppm Mn melt at equilibrium with $MnNb_2O_6$ is 52 ppm (Linnen and Keppler, 1997). At the same temperature, the empirical saturation model of Michaud and Pichavant (2020) yields 55 ppm Nb and 43 ppm Ta for a 500 ppm Mn and 2000 ppm Fe melt saturated with C-T with at. Mn/(Mn+Fe) = Ta/(Ta+Nb) = 0.5. For Beauvoir temperature and melt compositions, Linnen (1998) estimated a concentration of 50 ppm Ta at saturation with $MnTa_2O_6$, increasing to 1200-3000 ppm Ta and 40-100 ppm Nb at saturation with $MnNb_2O_6$ if the influence of Li and F melt concentrations on C-T solubility is accounted for. Although the calculations above do not all agree with concentrations measured in experimental Beauvoir glasses (38-49 ppm Nb, 20-34 ppm Ta, Table 9), most, in particular for Nb, are in the same range. Considering the uncertainties in the calculations and simplifying assumptions involved, this is taken as permissive evidence that our Nb and Ta glass concentrations represent C-T solubilities. The observed Nb and Ta enrichments with decreasing f (Fig. 9) would thus reflect a C-T solubility increase resulting from progressive melt fractionation during crystallization (higher F, P, Li, Fig. 4; 9).

Sn is an essential structural component in cassiterite (SnO_2), another accessory phase present in the charges and, so, Sn melt concentrations should reflect cassiterite solubilities (Linnen et al., 1995; 1996; Bhalla et al., 2005). Extrapolating to lower temperatures the data of Bhalla et al. (2005) at NNO+2.3 (vs. ~NNO+3 in our experiments), the solubility of cassiterite at 600°C is 120 ppm Sn, i.e. ~4 times higher than the measured Sn glass concentrations (between ~15 and ~35 ppm, Table 9). We also note the marked Sn depletions in B2N-25 and B2N-18 glasses and the global absence of Sn enrichment in the melt (Fig. 9). Sn alloying with the Au capsule (Linnen et al., 1995; Michaud et al., 2021) is probably responsible for Sn glass concentrations at cassiterite saturation being lower than calculated solubilities. Additionally, the high Li-mica and hematite Sn concentrations indicate that Sn is compatible at ~NNO+3 (see also below).

Several elements have concentrations that do not increase in the melt when decreasing f. This is the case for Mn which, following initial enrichment, returns to melt concentrations not much different from the initial C_0 for $f \sim 50\%$ (Fig. 9). Such a behavior could reflect increased Mn sequestration by Li-Mi at low f (see partition coefficient in Michaud and Pichavant, 2020) although Mn melt concentrations also depend on accessory phase solubilities, as it is an essential structural component in CT. Zn is neither significantly enriched nor depleted and Ti shows a similar although more irregular behavior (Table 9). The only element regularly depleted in the melt upon decreasing *f* is Sr. C/C_0 is 0.37 (*f* ~75%) and 0.27 (*f* ~50%) and the Sr data can be approximately fitted by Rayleigh fractionation for D = 3 (Fig. 9) thus indicating a marked compatible character during crystallization of Beauvoir melts. In comparison, Pb is more irregular than Sr although a depletion trend appears if the anomalous concentration in charge B2N-18 (Table 9) is discarded. The Ba and La systematics are unclear because of their very low melt concentrations, as discussed above.

Experimental Qz crystals were analyzed only in B2N-25 because of size limitations (Fig. 1a). Five analytical spots were performed. Only one yielded a stable signal during almost the entire ablation time interval before finally the underlying glass was hit. This Qz has 81.34 ppm Li, 367.92 ppm Al and 152.94 ppm P (not corrected for possible interferences, Audétat et al., 2014) and it contains Ti, Zn, Sn and Cs concentrations in the few ppm range (Table 9).

Mineral/melt partitioning

The distribution of F between mica and melt is strongly concentration dependent (Fig. 10). Below ~3 wt% F in melt, an approximately linear dependence is observed between F in mica vs. F in melt with a slope of ~1.4 (30 data points). F is therefore preferentially partitioned in Li-Mi than in silicic melt, consistent with previous results (Kd Mu/L = 1.8, Icenhower and London, 1995; 0.94-1.56, Pichavant et al., 2016). Above ~3 wt% F in melt, F concentrations in mica increase drastically. This goes along with important changes in mica crystal chemistry toward a more marked trioctahedral character. The F Kd Li-Mi/L reaches values between 2 and 3, in the range of biotite-liquid F partitioning data (Kd Bt/L = 2.3, Icenhower and London, 1997; average of 2.3, Pichavant et al., 2016). Therefore, F partitioning closely follows the major element composition and structure of the mica. No attempt was made to constrain the distribution of Li between mica and melt since in this study Li concentrations in micas are calculated (see above).

The trace element data in charge B2N-25 allow the Qz/L partition coefficients for Li, Al, P, Ti, Zn, Sn, Cs, W to be estimated (Table 9). For Li, the experimentally determined partition coefficient (0.027) is significantly lower than calculated from the Yellowstone tuffs (~0.073, Neukampf et al., 2019) and the Macusani volcanics (0.17, Michaud and Pichavant (2020).

Sn concentrations in charge B2N-25 yield very high partition coefficients for Li-mica and hematite (Kd Li-Mi/L ~170 and Kd Hm/L ~890 respectively) using the separate Sn analyses of Li-mica and hematite reported above and the glass analysis from Table 9. These partition coefficients represent maximum values because Sn was progressively lost from the melt to the capsule. However, Kd Li-Mi/L from this study is markedly higher than previous muscovite/L partitioning data (0.38-0.49, Raimbault and Burnol, 1998; 0.48-0.49, Michaud and Pichavant, 2020) implying that Sn is compatible in micas under our experimental conditions. Given the high fO_2 of the B2N-25 experiment (~NNO+3), tin should be present as Sn^{4+} (Linnen et al., 1995; 1996) and the very elevated Kd Li-Mi/L from this study suggests that Sn^{4+} preferentially partitions in mica rather than in melt.

DISCUSSION

Evaluation of kinetic issues

In this study, crystallization experiments have been conducted at temperatures uncommonly low (down to ~550°C, Table 2; 3) for silica-rich melt compositions and, so, an evaluation of kinetic issues is particularly necessary. Silicic crystal-melt systems have been known for long to be difficult to equilibrate. In crystallization experiments, supercooling is of general concern and, in melting experiments, superheating can be necessary to overcome the sluggish dissolution kinetics of some phases, in particular quartz (Piwinskii and Martin, 1970; Pichavant et al., 1987a and references therein).

Several observations indicate kinetic difficulties in our experiments despite the long experimental durations. The most critical concerns saturation temperatures for major phases at 100 MPa which are lower than at higher pressures under water-saturated conditions (see above), a behavior symptomatic of supercooled melts. The effect of melt supercooling is to delay phase appearance for a given temperature and/or shift phase appearance to a lower temperature for a given experimental duration. In supercooled charges which contain proportions of crystals lower than equilibrium, melts compositions can be metastable. Results of melting experiments (Pichavant et al., 1987a; Table S4) confirm the very low saturation temperatures in the 100 MPa crystallization experiments. Qz saturation temperatures are lower by <115°C in crystallization than in melting experiments on B1, and by 85°C on B2 (Fig. 2; 3). For Pl, differences between melting and crystallization saturation temperatures are <80°C for B1 and 55°C for B2 (Fig. 2; 3). Af in crystallization experiments saturate at temperatures 20°C lower than in melting experiments and, for Mu, the two saturation temperatures are within +/-5°C of each other (Fig. 2; 3). Therefore, the 100 MPa crystallization experiments underestimate the Qz and Pl saturation temperatures and also slightly the Af. We stress that this does not necessarily imply that saturation temperatures from melting experiments approach equilibrium more closely because melting kinetics of major phases can be sluggish, particularly for Qz as noted above.

In contrast, at 300 MPa for B2, Pl, Af and Li-Mi saturation curves in crystallization and melting experiments are within 5°C of each other (Fig. 3). Qz is the only major phase whose saturation temperature could be slightly underestimated since it persists up to 40°C higher in melting than in crystallization experiments (Fig. 3). In the 200 MPa B2 experiments, all major phases saturate at temperatures consistent with those at 300 MPa (Fig. 3). For B1, saturation temperatures are all higher in crystallization than in melting experiments, most probably because of the low sensitivity of the X-ray phase identification method used in the melting experiments (Pichavant et al., 1987a). Therefore, there is no indication that equilibrium is not approached in the 300 MPa B1 crystallization charges. We conclude that melt supercooling issues in this study mainly concern the 100 MPa and are minor or absent in the 200 and 300 MPa charges. Such a marked influence of pressure is most probably due to the significantly higher melt H2O concentrations at 300 and 200 than at 100 MPa which would speed up crystallization kinetics at high pressures.

Major element compositions of major phases provide additional insights on equilibrium states. Although the glasses are chemically homogeneous, some specific compositions might correspond to metastable melts. This includes the 100 MPa glasses which have normative Qz higher than the other glasses (Fig. 5) and could be too SiO_2-rich because of Qz proportions less than equilibrium. Similarly, the distinctive normative Or-rich composition of B2N-18 glass (Fig. 5) could indicate delayed Af appearance. The observation that feldspar pairs mostly correspond to compositions at equilibrium on the ternary solvus (Fig. 6) does not necessarily imply that all phases in our experiments reached equilibrium compositions. The heterogeneous feldspars (and their compositions inside the solvus) and the Al-rich quartz solid solutions are interpreted as remnants of non-equilibrium compositions still present in some charges despite long experimental durations.

Natural feldspar and mica compositions

At the difference of the melting experiments where mineral assemblages and compositions are inherited from the starting granites (Pichavant et al., 1987a), experiments from this study provide information on compositions of phases crystallizing from B1 and B2 melts. This allows crystallization of the Beauvoir granite to be reconstructed and compositions of major mineral phases, mainly feldspars and micas, in the granite to be interpreted in the light of experimental results.

Averages of natural feldspar compositions along the GPF drill core ($Or_1Ab_{98.5}An_{0.5}$ for plagioclase, n = 69 and $Or_{90}Ab_{10}$ for K-feldspar, n = 42, Johan et al., 1988) are very close to compositions in our starting rocks (Fig. 6). Only 5 plagioclases have > 1% An (maximum 2.5) and 3 have > 1.5% Or (maximum 7.4, Johan et al., 1988). In comparison, experimental Pl have An mostly > 1% and are much more K-rich (~10% Or) than the natural compositions (Fig. 6). Natural K-feldspars range from Or_{87} up to Or_{100} and only one composition (Or_{78}, Johan et al., 1988) approaches the Af experimental range (Or_{67-73}, Fig. 6). The natural feldspar pair in the starting rocks yields equilibration temperatures of 391 and 407°C for pressures of 100 and 300 MPa respectively (Wen and Nekvasil, 1994) and, therefore, their compositions were frozen ~150°C colder than the Beauvoir solidi (Fig. 2; 3). Clearly, most feldspars do not preserve magmatic compositions. However, a few rare analyses (the most An- and Or-rich Pl and the most Na-rich Af) suggest that primary compositions were close to the experimental ranges. We conclude that feldspars in the Beauvoir granite have been extensively re-equilibrated during the post-magmatic evolution.

Several mica crystallization stages have been recognized in the Beauvoir granite. The earliest corresponds to relatively Li-poor Fe-bearing Li-Mi (Li-, Fe-muscovites of Kosakevitch, 1976) subsequently interpreted as near-liquidus phases from relatively unfractionated melts (Monier and Tegyey, 1985; Monier et al., 1987). These compositions are quite rare and represented in our dataset by only one EMPA analysis (the right most in Fig. 7b). They have not been exactly reproduced in the experiments, and the B2 Li-Mi compositions have Mg-Li slightly higher than early stage micas (Fig. 7a; b). The main stage is characterized by the crystallization of Li-, F-rich zinnwaldites to polylithionites which postdate the early stage compositions and have been previously interpreted as crystallized from fractionated sub-liquidus melts (Monier et al., 1987). This mica crystallization stage has been adequately simulated by the B1 experiments where Li-Mi compositions are closely similar to the natural Beauvoir micas (Fig. 7).

The evolution of Beauvoir micas from early Li-poor Fe-bearing Li-Mi to zinnwaldites and polylithionites (increasing $Fe_t + Mn + Ti - Al^{VI}$ with decreasing $Mg - Li$) parallels the compositional shift of experimental micas from the B2 to the B1 charges. This trend ((1) in Fig. 7a) is positively correlated with the melt F content (Fig. 8). It describes the compositional evolution of Li-Mi crystallizing from a progressively more F-rich peraluminous granitic melt. The mica becomes more silicic, less aluminous and its trioctahedral character increases, a general evolution which can be understood from the structural role of F in aluminosilicate melts (increase of a_{SiO2}, complexing between F and Al, Manning, 1981; Xiong et al., 1998; 1999). The F control of experimental mica compositions along trend (1) is also marked in PHP rare metal granites. In the Argemela intrusion which contains significantly less F than Beauvoir (0.5-1.0 wt% F, Michaud and Pichavant, 2020), most micas plot at the high Mg-Li end of trend (1), in the same domain as experimental B2 micas (Fig. 7a; b). Thus, Beauvoir melts with F contents intermediate between our two starting compositions would be expected to crystallize Li-Mi filling the gap between the B1 and B2 experimental compositions, in the range inferred for the early stage micas. Another evolutionary trend ((2) in Fig. 7a and 8) is apparent both in natural and experimental micas. $Fe_t + Mn + Ti – Al^{VI}$ decreases with decreasing Mg – Li as illustrated by the Beauvoir mica separate data (Fig. 7b) and by the experimental compositions from B1N-23, -22 to -21 (i.e., upon decreasing temperature and melt fraction, Fig. 4; 7a; 8). This trend is a mica fractionation trend, i.e., it reflects the removal and progressive exhaustion of mafic components from the F-rich peraluminous granitic melt as mica crystallizes. The observed zonation of mica compositions across the GPF drill core (zinnwaldites at the base and polylithionites at the top, Monier et al., 1987) is consistent with crystallization from a more fractionated melt in the latter than in the former case. We conclude that the composition of Beauvoir micas preserves two distinct magmatic evolutionary trends (Fig. 7a).

However, several mica chemical features do not fit in an entirely magmatic interpretation. Micas from the B1 unit have FeO_t and MgO concentrations (respectively < 1 and < 0.1 wt%, Monier et al., 1987) much lower than in B1 charges (~1-5.5 and ~0-2 wt% respectively, Table 7; S3). Conversely, MnO concentrations in natural micas are higher (on average ~0.8 wt% and up to ~1.5 wt% MnO in the B2 unit, Monier et al., 1987) than in experimental micas (0-0.4 wt%, Table 7; S3). This suggests that FeO_t, MgO and MnO in micas do not represent magmatic concentrations and have been modified by post-magmatic fluid circulations.

Redox conditions and magmatic F, Li concentrations

The presence of hematite and magnetite in our experiments constitutes the main point of divergence between the experimental and natural phase assemblages since the Beauvoir granite contains no Fe-Ti oxide except secondary rutile (e.g., Monier et al., 1987; Cuney et al., 1992). Below, we exclude the possibility that Fe-Ti oxides were once present but all completely destroyed during late-stage crystallization processes, either magmatic or post-magmatic. Therefore, the lack of Fe-Ti oxides in the granite can be used to constrain the redox conditions. In our experiments, hematite was found in the most oxidizing (~NNO+3) and magnetite in less oxidizing (NNO+1) charges (Lahlafi, 1997). It is recalled that no Fe-Ti oxide crystallized in the NNO-1 and NNO-1.4 experiments. This constrains the fO_2 of the Beauvoir granite to a range more reducing than NNO+1 and more oxidizing than NNO-1.4 since Bt would be present under such highly reducing conditions (Table 3), which is not observed (Cuney et al., 1992). Previously, an oxidizing magmatic evolution has been recognized at Beauvoir (Cuney et al., 1992 and see the Ta, Nb, Sn mineralization section below). A progressive oxidizing trend is developed at the scale of the GPF drill core, superimposed on more reducing conditions as demonstrated by lepidolites with low Fe^{3+}/Fe^{2+} at the base, presence of uraninite in B3 and B2 (Cuney et al., 1992) and absence of Fe-Ti oxides in the lower granite units. Therefore, the < NNO+1 to > NNO-1.4 range inferred from our experiments is interpreted as representative of early magmatic conditions. This implies that most of our crystallization experiments have been performed at an inappropriately oxidizing fO_2. This has minor consequences for the stability of major phases since varying fO_2 from ~NNO+3 to NNO-1 has no systematic influence on the location of saturation curves (Fig. 2; 3). However, fO_2 has definitely an influence on phase compositions (see above the Fe and Sn contents of experimental micas). The specific behavior of some trace elements (compatible for Sn and strongly incompatible for U, Fig. 9) also reflect the oxidizing conditions of most of our experiments.

Crystallization of topaz and amblygonite in experiments from this study provides unambiguous confirmation that both can be magmatic phases in the Beauvoir granite (Monier and Tegyey, 1985; Rossi et al., 1987; Cuney et al., 1992). Previously, topaz has been reported to be present in early crystallization experiments. However, topaz identification was uncertain (see Pichavant et al., 1987a). In this study, topaz was identified by SEM and analyzed by electron microprobe. It appears only in charge B1N-21 at 580°C, 300 MPa which is one of the two most evolved B1 charges. Melt in B1N-21 has the highest F concentration (3.31 wt% if unnormalized) and one of the two highest normative Corundum (6.5%, Fig. 4; Table 4). The rarity of topaz in our experimental charges contrasts with its ubiquitous presence in the Beauvoir granite. Previous work has emphasized F and Li loss from the crystallizing magma and F concentrations as high as 4 wt% have been considered possible for Beauvoir melts (Cuney et al., 1992). An average F concentration of 4.9 wt% has been found in re-homogenized melt inclusions from the B1 unit (Kovalenko et al., 1998). Such F concentration levels are on average above our experimental melt concentrations although the most F-enriched B1 glasses approach the 4 wt% range, if normalized to 100% anhydrous (i.e., 3.70 wt% F for B1N-21). However, experimental topazes have elevated F concentrations (at. F/(F+OH) = 0.89-0.99, Table 8). This is higher than the old values from the GPF drill core (at. F/(F+OH) = 0.78-0.92, Monier and Tegyey, 1985) but in the range of recent data for topaz in the B1 unit (0.96-1.04) and in a dike associated with the B2 unit (0.93-0.94, L. Monnier, pers. comm. 2022). In other words, there is no indication that the F concentration in the B1N-21 experimental melt was much lower than in natural Beauvoir melts. In comparison, experimental F concentrations in B2 charges were probably insufficiently high given the relatively Li-, F-poor Li-Mi compositions crystallized in B2 (Fig. 7 and see above).

Topaz is a rather low temperature and late crystallizing phase in our experiments, appearing later than mica in the B1 300 MPa crystallization sequence. The data suggest that a minimum F content of 3-3.5 wt% in the melt is necessary for topaz to be stable (see also Soufi, 2021). In our experiments, such elevated F contents are reached in the sub-liquidus domain where quartz and feldspar crystallization enrich the residual melt in F (Fig. 4). The low topaz crystallization temperature observed in this study is consistent with at. F/(F+OH) ~1 in experimental topaz since at higher temperatures F partitions less favorably in topaz than in other phases (Soufi, 2021). In melts with F >> 3-3.5 wt%, topaz with at. F/(F+OH) < 1 is a high temperature near-liquidus phase (Xiong et al., 1999; Lukkari and Holtz, 2007). This is not what is observed at Beauvoir where topaz is a sub-liquidus low temperature phase and has at. F/(F+OH) ~ 1. We conclude that the rarity of topaz in our experiments is simply a reflection of the small number of low melt fraction charges available for the B1 composition (Fig. 4). At 580°C and 300 MPa, melt fractions are still high (f=67 wt% in the topaz-bearing charge B1N-21, Table 3) so that, during the crystallization of the last (>50 wt%) B1 melt fraction, topaz should be present. Under these conditions, the melt F content should also reach the 4 wt% level typical of the B1 unit (Cuney et al., 1992; Kovalenko et l., 1998).

Experimental amblygonites from this study are richer in F (~13 wt% F, Table 8) than their natural counterparts in the Beauvoir granite (~10.5-11.5 wt% F, London et al., 2001). Yet, it is possible that amblygonites from the more evolved B1 and B2 units have higher F contents since the data above (from Ph. Rossi) are for the B3. Apatites in experiments and in the GPF drill core (Johan et al., 1988; Cuney et al., 1992) are both F-rich, the natural having generally higher MnO concentrations (~3 to ~6 wt%) than the experimental compositions (Table 8). In conclusion, the range of F melt concentrations generated in our B1 charges is in the range or slightly lower than in the natural magma. However, the B2 experiments probably underestimate the F concentrations in the natural magma. In fact, our starting B2 sample, although stratigraphically from the B2 unit, has geochemical characteristics typical of B'2 compositions (high SiO_2 and low Al_2O_3, P_2O_5 and F, Raimbault et al., 1995). This explains our experimental results in particular the relatively Li-, F-poor compositions of Li-Mi crystallized in B2 (see above).

Crystallization and conditions of emplacement of the Beauvoir granite

Results from this study confirm the very low magmatic temperatures of the Beauvoir granite. Further to the solidi previously discussed (Fig. 2; 3; Pichavant et al., 1987a), the 100 MPa liquidus temperatures are 715°C for B1 and 720°C for B2 (from the melting experiments because of melt supercooling in the 100 MPa crystallization experiments) and the 300 MPa > 640°C for B1 (620°C from the melting experiments) and 640°C for B2 (670°C from the melting experiments). Thus, in the 100-300 MPa range, the two Beauvoir compositions studied begin to crystallize at temperatures lower than the H_2O-saturated haplogranite solidus (Tuttle and Bowen, 1958; Fig. 2; 3). Such magmatic conditions are exceptional and only approached by flux-rich granitic compositions (Xiong et al., 2002; Lukkari and Holtz, 2007; Aksyuk et al., 2016), granitic pegmatites (Burnham and Nekvasil, 1986) and by the Macusani glass (Pichavant et al., 1987b; London et al., 1989).

Two types of experimental results suggest that the B1 and B2 granite units have the significance of crystallized liquids. First, the four major phases (Qz, Pl, Af, Li-Mi) saturate in very narrow temperature intervals, both in B1 and B2 (Fig. 2; 3). Saturation temperature intervals are of 20-30°C at 100 MPa, probably a consequence of melt supercooling, and of 30-40°C at 300 MPa. Thus, liquidus temperatures are only a little higher than temperatures of multiple saturation of the melt with the four major phases. This requires that the B1 and B2 starting granites are compositionally close to their respective multiply saturated melts. Second, residual melts in both the B1 and B2 charges little depart from their respective starting compositions (Fig. 5). Deviations are within 2-3% normative, at the exception of a few charges (the 100 MPa, B2O-38/40, B2N-18, Fig. 5) discussed previously. Such a behavior again requires that compositions of liquidus and multiple saturation melts are close to each other and, so, the two starting compositions must represent essentially frozen liquids.

This result opens perspectives for constraining the crystallization pressure of Beauvoir melts. Experimental data are available on the influence of pressure (under water-saturated conditions, Tuttle and Bowen, 1958) and of additional components at constant pressure (F, Li, P, A/CNK, (F: Manning, 1981; Li: Martin, 1983; A/CNK: Holtz et al., 1992a; b; P: London et al., 1993) on the location of minima and eutectics in the haplogranite system (Fig. 5).

However, the combined effect of these different variables is as yet undetermined. As an illustration, the F-rich B1 and B2 compositions plot at normative Quartz contents significantly above the minimum liquidus points with added F at 100 MPa (Manning, 1981; Fig. 5). This is attributed to the influence of very high A/CNK and normative Corundum in Beauvoir melts (Holtz et al., 1992a; b). Therefore, pressures of Beauvoir melt crystallization cannot be constrained directly from the reference liquidus points presently available. Melts multiply saturated with the four major phases at 300 MPa plot closer than at 100 MPa to their respective starting compositions which would tend to suggest that 100 MPa is too low a pressure for early crystallization. However, the 100 MPa melts probably represent metastable compositions (see above). We must conclude that no reliable barometric information can be presently extracted from the major element compositions of Beauvoir granites.

Petrographic observations and textural evidence have shown that albite and lepidolite are the two earliest major phases to crystallize in Beauvoir magmas (Kosakevitch, 1976). Mica is earlier than albite in some samples but the reverse is observed in others and, so, the two phases can be considered to appear almost together on the liquidus. Quartz, frequently euhedral and with albite inclusions present in external growth zones (M. Cuney, personal communication, 2022), is also an early phase, being followed by K-feldspar. By reference to the P-T diagrams, these textural relations require that crystallization started at pressures > 300 MPa for B1 and at ~200-250 MPa for B2 (Fig. 2; 3). Final solidification of the pluton took place at its emplacement level (~ 80 MPa from the P-T conditions of exsolution of the magmatic fluids, Cuney et al., 1992). Therefore, pressures of early (> 200-250 MPa) and final crystallization (80 MPa) are significantly different and Beauvoir melts started to crystallize at depths higher than their emplacement level. Since they represent crystallized liquids, this implies that little melt-crystals segregation took place during final ascent.

Fractionation in the Beauvoir granite

The major and trace element zonation observed among the different Beauvoir granite units has been used as a reference example of chemical fractionation in rare metal granites (Zhu et al., 2001; Costi et al., 2009; Cuney and Marignac, 2015; Pollard, 2021). Although mechanisms of fractionation in rare metal granites and pegmatites are still debated, this study demonstrates that most of the distinctive mineralogical and geochemical characteristics of the Beauvoir granite result from magmatic rather than hydrothermal post-magmatic processes. Albitic plagioclase, Li-, F-rich mica, topaz and amblygonite are of magmatic origin. A/CNK, F and P_2O_5 concentrations increase and trace elements fractionate as a result of progressive crystallization (Fig. 4; 9).

The major element signature of fractionation at Beauvoir is examined by comparing granite whole rock and experimental glass compositions (Fig. 11). The granite units globally define a progressive fractionation trend marked by increasing A (= 1000 (Al – (Na + K + 2Ca) at.) at decreasing B (=1000 (Fe+Mg+Ti) at., Fig. 11a). This natural trend, classical for rare metal granites (Linnen and Cuney, 2005; Cuney and Marignac, 2015), is well reproduced by the experimental data (Fig. 11b) and this confirms that Beauvoir granites are reliable proxies for magmatic liquid compositions. In the Q*3-B*3-F*3-M*3 representation, all granite compositions plot close to each other but the two groups of experimental glasses define fractionation trends marked by increasing M*3/F*3 at constant Q*3 (Fig. 11c; d). These trends match with the evolutions at constant normative Quartz contents in the Qz-Ab-Or diagram (Fig. 5) and with the increase in normative Corundum with decreasing melt fraction and progressive fractionation (Fig. 4). The 100 MPa glasses again deviate from the trends, being distinctly shifted toward Q*3-rich compositions (Fig. 11d). We note that the two B1 and B2 glass fractionation trends do not coincide (Fig. 11b; d) as observed in the Qz-Ab-Or diagram where the B1 and B2 data points plot in different fields (Fig. 5). The two B1 and B2 trends also remain separate from each other when plotted as a function of melt fraction (Fig. 4). Therefore, the B1 and the B2 samples do not belong to the same evolutionary trend and this demonstrates that our two Beauvoir starting compositions are not comagmatic. Reminding that our B2 starting rock has geochemical attributes of B’2 compositions, the experimental glasses thus confirm previous conclusions from whole rock data that the B and B’ represent two distinct magmatic series (Raimbault et al., 1995). Experimental data are lacking to discuss the mutual relationships within the B series, i.e., between the B1, B2, B3 compositions which are geochemically close to each other (Raimbault et al., 1995; Fig. 11c). A progressive decrease in normative Quartz is observed at the scale of the GPF drill core from the B3, B2 to the B1 units, positively correlated with an increase of the F content (Cuney et al., 1992). This evolution has been attributed to the role of F on granite phase equilibria (Manning, 1981; Cuney et al., 1992) although other components (Li, P, A/CNK) must also be involved (see above, Fig. 5). However, the important point to be emphasized is that this geochemical variability among the B units is not generated at the emplacement level of the intrusion because differentiation of Beauvoir melts yields derivative products with almost constant normative Quartz (Fig. 5; 11). Therefore, our results suggest that the B1, B2 and B3 granite units represent three independent magma batches generated at depth.

Trace element fractionation generated in experiments from this study are compared with those observed in Beauvoir granites (Fig. 12). For most elements, the data points plot in the upper right and lower left quadrants and so most elements fractionate (become either enriched or depleted) similarly in experiments and from B2 to B1. This strongly suggests that magmatic crystallization is at the origin of the trace element fractionations observed at Beauvoir. Elements enriched include Li, Be, U, F, P, Rb, W while Sr, Pb are depleted. The former group plots close to the 1:1 line (except Be, Fig. 12) and so, for these elements, the experimentally generated enrichments are similar in magnitude to those observed from B2 to B1. Cs is an exception (enriched in the experiments but depleted from B2 to B1) explained by the high Cs concentration in our B2 starting sample (Raimbault et al., 1995). For Sr and Pb, the experimental depletions are respectively higher and lower than from B2 to B1. Ti is significantly fractionated neither in the experiments nor in the granites (Raimbault et al., 1995). Zn and Mn plot close to the vertical axis (Fig. 12) and so they do not fractionate in the experiments (Fig. 9), although both are depleted from B2 to B1 (Raimbault et al., 1995). However, the significant variations of whole rock Mn concentrations in the top part of B1 (where a 20 m Mn-enriched “fringe zone” overlies a Mn-depleted level of about the same thickness, Raimbault et al., 1995) and the observation that the natural lepidolites and apatites are generally richer in Mn than their experimental counterparts (see above) suggests Mn re-distribution during cooling of the intrusion.

Origin of the Beauvoir granite

The constraints placed on the evolution of the Beauvoir granite raise the question of its origin. There is agreement that it is ultimately related to the tectonic evolution, thermal maturation and partial melting of the continental crust during late Variscan times (e.g., Gebelin et al., 2009; Lardeaux, 2014; Augier et al., 2015; Barbey et al., 2015). In this framework, the genesis of highly fractionated granitic melts such as Beauvoir can be accounted for by two possible models (1) extreme differentiation from less evolved crustal parental magmas (e.g., Raimbault et al., 1995; Cerny et al., 2005b; London, 2008; Hulsbosch, 2019) or (2) direct anatectic origin (e.g., Stewart, 1978; Christiansen et al., 1986; Cuney and Autran, 1987; Nabelek et al., 1992a; b; Muller et al., 2017). In fact, results of this study do not favor any of these two models. The thermal characteristics of Beauvoir melts (liquidus temperatures of 670°C maximum at 300 MPa) make it possible that they represent near-solidus residual melts from the crystallization of parental peraluminous leucogranitic magmas (e.g., Scaillet et al., 1995). Alternatively, these liquidus temperatures are within the P-T evolution of metamorphic units during late Variscan times and appropriate for crustal melting either under fluid-absent (muscovite-dehydration melting) or fluid-present (Cuney and Autran, 1987; Gardien et al., 1997; Lardeaux, 2014; Augier et al., 2015; Barbey et al., 2015; Michaud et al., 2021). Although an origin of rare metal granites by fluid-absent melting of residual lithologies previously enriched by the removal of a low-temperature melt fraction has been commonly proposed (see Michaud et al., 2021), this model can be discarded for Beauvoir since it would imply melt generation at temperatures much higher (at least 100°C higher for biotite-dehydration melting) than the B1 and B2 liquidi.

Geological evidence in support of any of the two models is ambiguous. At Beauvoir, there is no candidate parental magma exposed (it would likely be represented by granitic units intermediate between the Beauvoir and Colettes) but other granites are probably present at depth (Aubert, 1969; Cuney and Marignac, 2015). The anatectic model (Cuney and Autran, 1987) has been ruled out on a geochemical basis (Raimbault et al., 1995). However, updated versions of the model have been recently elaborated (Cuney and Barbey, 2014). We also note that the differentiation model called for initial melts slightly enriched in rare metals (Sn and W) originated from geochemically specialized lower crustal sources (Raimbault et al., 1995). Differentiation, postulated to start at the anatexis level, generated strongly peraluminous, F- and P-bearing and rare metal enriched melts (Raimbault et al., 1995). Further differentiation during ascent led to the individualization of the B and B' magma series, the B1 and B2 units representing two variably differentiated liquids from the same B magma and the B3 possibly a slightly cumulative part of the B2 (Raimbault et al., 1995).

Our experimental results confirm that the Beauvoir intrusion was built from at least two distinct magmatic batches (see above, Fig. 11), all strongly peraluminous, P- and F-rich and with elevated rare metal contents. They stress the importance of deep-seated fractionation processes rather than those occurring in situ at the emplacement level. We note that the fractionation mechanisms supporting the differentiation model are still poorly defined. For example, amplification of melt structure and viscosity fluctuations during ascent has been proposed to promote dynamic separation between more evolved less polymerized and less evolved more polymerized melts (Raimbault et al., 1995). A combination of Bagnold effect and filter-press processes has been suggested to control fractionation during ascent of rare metal granitic melts in dykes (Marignac et al., 2009; Cuney and Marignac, 2015). These mechanisms need further testing and validation and we conclude that the origin of the Beauvoir melts still requires more work.

Ta, Nb, Sn mineralization

Ta and Nb are both enriched although much more in granites than in experiments as indicated by their position well above the 1:1 line (Fig. 12). The experimental Ta and Nb contents (maximum 34 ppm Ta and 49 ppm Nb, Table 9) stay globally in the range of B2 concentrations (~45 ppm Ta and ~50 ppm Nb, Raimbault et al., 1995). They do not reach the high to very high values observed in B1, ~150 ppm Nb and up to ~450 ppm Ta in the upper "fringe zone" (Raimbault et al., 1995). C-T solubility data (Linnen and Keppler, 1997; Linnen, 1998; Van Lichtervelde et al., 2018) have demonstrated higher solubility limits for the Ta than for the Nb C-T end-members which provides an explanation for the fractionation of Ta over Nb and the preferential Ta enrichment observed in B1. They also stress the importance of the melt Li and F concentrations in controlling C-T saturation in rare metal magmas. In this respect, it is worth emphasizing that our trace element data concern the B2 magma only. Fractionation in B2 charges increases F, P, Li (Fig. 4; 9) which leads to a C-T solubility increase responsible for the Ta and Nb enrichments observed in residual melts (Fig. 9). Fractionation in B1 generates melts more F-, P- and presumably more Li-rich than in B2 (Fig. 4). Thus, Ta and Nb melt concentrations at C-T saturation higher than in B2 charges can be expected and it is possible that residual B1 melts would have Ta and Nb approaching the concentration levels observed in the B1 unit. This interpretation is consistent with a magmatic control of the Ta and Nb mineralization at Beauvoir (Raimbault et al., 1995).

For Sn, the strong enrichment observed in granites (B2: 300-800 ppm; B1: 800-1600 ppm, Raimbault et al., 1995) has no counterpart in experimental melts (Fig. 9; 11). In the ~NNO+3 charges, Sn melt concentrations are controlled by cassiterite crystallization, Sn partitioning toward Li-Mi and Hm and Sn loss to the capsule. In Beauvoir granites, Sn is carried mainly by magmatic cassiterite implying that Beauvoir melts became cassiterite-saturated at some point during their evolution. Sn whole rock concentrations and their variations within and between units mainly reflect the proportion of cassiterite crystals which, at cassiterite saturation, is controlled by the Sn content of the initial melt (a high Sn melt will produce a higher amount of cassiterite than a low Sn melt when brought at cassiterite saturation). Experimental data have shown that cassiterite solubility mainly depends on fO_2 at a given temperature and melt A/CNK, the influence of F being negligible (Bhalla et al., 2005 and references therein). Cassiterite solubilities are of the order of 100 ppm at NNO+2-3 but increase rapidly to the several 1000 ppm range or more under reducing conditions (Bhalla et al., 2004 and references therein). Therefore, magmatic oxidation is a very efficient mechanism to promote cassiterite saturation (Linnen et al., 1995; 1996; Pichavant et al., 2016). At Beauvoir, several lines of evidence for a late progressive oxidation of the intrusion have been presented (Cuney et al., 1992 and see the redox section above). This promoted cassiterite saturation in melts enriched in Sn by crystallization-differentiation at the intrusion level (Michaud and Pichavant, 2020). Sn contents of initial melts are unknown but can be estimated to be of a few hundred ppm for B2 or more for B1, considering the respective whole rock concentrations. Some Sn was extracted and transported by postmagmatic hydrothermal fluids as suggested by the Sn depletion in the upper part of the cupola (Cuney et al., 1992; Raimbault et al., 1995). The final Sn distribution in the intrusion was probably controlled by the re-mobilization by late postmagmatic fluids of Sn from cassiterite and Sn-bearing micas.

Broader implications for granitic magmatism

One important result from this study is the confirmation of the very low magmatic temperatures of the Beauvoir granites (see above). This demonstrates that natural granites solidi are in fact quite variable. Many (Burnham and Nekvasil, 1986; London et al., 1989; Xiong et al., 2002; Lukkari and Holtz, 2007; Aksyuk et al., 2016; this study) are much colder than the H2O-saturated haplogranite solidus (Tuttle and Bowen, 1958). It is important to consider the latter as a theoretical reference rather than as a universal benchmark for the solidus of granitic rocks (see Ackerson et al., 2018).

Two-feldspar thermometry and more recent geothermobarometric methods such as Ti-in-quartz generally have yielded temperatures between 400 and 600°C for the crystallization of granitic rocks (Moazzen and Droop, 2005; Glazner and Johnson, 2013; Ackerson et al., 2018; London et al., 2020). Despite the particularly low solidus temperatures for Beauvoir, albite and K-feldspar record equilibration temperatures that are still ~150°C colder (see above). These subsolidus equilibration temperatures have led to speculations on mechanisms of final consolidation of granitic bodies (Ackerson et al., 2018). By far the most likely explanation is that such low crystallization temperatures indicate fluid-assisted mineral re-equilibration during the post-magmatic evolution, the interpretation proposed above for Beauvoir and other granites (Moazzen and Droop, 2005; Lukkari and Holtz, 2007). For example, feldspars experience major chemical, textural and structural transformations during the cooling of granitic bodies (Parsons, 1978; Smith and Brown, 1988). These reactions are triggered by fluid percolation and fluid-rock interaction as demonstrated by fluid inclusions (Kontak et al., 1984) and stable isotope studies (Taylor and Forester, 1971; Fouillac and Rossi, 1991). Both quartz and feldspars in the GPF drill core show a systematic decrease in

$\delta^{18}O$ from base to top, interpreted to indicate interaction with meteoric fluids at high temperature (Fouillac and Rossi, 1991; Cuney et al., 1992). Thus, despite its exceptionally low solidus temperature which makes the post-magmatic “window” narrower, the Beauvoir granite reminds us of the importance of re-equilibration processes involving hydrothermal fluids in the final solidification of granitic plutons.

CONCLUSIONS

Crystallization experiments performed on two Beauvoir granite samples (B1 and B2) simulate the magmatic evolution and chemical fractionation in strongly peraluminous, F- and P-rich rare metal magmas. The main conclusions of the study are the following:

- Beauvoir melts crystallize a magmatic assemblage which includes quartz, albitic plagioclase, K-feldspar, Li-mica, apatite, cassiterite and columbo-tantalite. This assemblage, joined by topaz and amblygonite in the B1 experiments, closely reproduces the granite mineralogy. Fe-Ti oxides are present for fO_2 between ~NNO+3 and NNO+1.

- The crystallization experiments confirm the very low solidus temperatures of the granites. In the 100-300 MPa range, B1 and B2 have liquidus temperatures lower than the H_2O-saturated haplogranite solidus, an exceptional behavior characteristic of flux-rich granitic melts.

- Upon progressive crystallization, residual melts become more F- and P-rich. Melt major element compositions evolve at constant Qz contents and become more peraluminous. F-rich topaz and amblygonite crystallize as sub-liquidus phases from these evolved melts.

- Comparison between natural and experimental mineral compositions suggest that feldspars in the granite have been re-equilibrated during the post-magmatic evolution. Both natural and experimental micas follow similar trends from Li phengites to zinnwaldites and polylithionites. Compositions closely similar to the natural Beauvoir micas crystallize in the B1 experiments.

- The fO_2 ranged from < NNO+1 to > NNO-1.4 during the early magmatic stage, later evolving to highly oxidizing conditions at the magmatic-hydrothermal transition. F, Li melt concentrations in B1 experiments reproduce or are slightly lower than the concentrations in the natural magma. Those in B2 underestimate most natural B2 concentrations since the starting sample has geochemical attributes of B’2 compositions. Glass major elements suggest that our two starting compositions are not comagmatic. The major distinction between the B and B’ geochemical series at Beauvoir is confirmed. The intrusion was made from at least two independent magma batches.

- The low liquidus temperatures, narrow saturation temperature intervals and grouped residual melts imply that the Beauvoir granites represent crystallized liquids. Beauvoir melts started to crystallize at depths (≥200 MPa) significantly higher than their emplacement level (80 MPa). Our results stress the importance of deep-seated processes (either partial melting or differentiation) as a way to generate the specific major element compositions of Beauvoir melts.
- Upon magmatic crystallization, the melt becomes enriched in Li, Be, B, Rb, Cs, W, U, Nb, Ta and depleted in Sr and Pb. Fractionation trends observed in Beauvoir granites are similar to those in experiments suggesting that crystallization at the emplacement level controls chemical fractionation for most elements.
- Sn is compatible in micas and hematite under highly oxidizing conditions. This, together with cassiterite crystallization and Sn loss, prevents Sn enrichment in residual melts. Cassiterite saturation in Beauvoir magmas was promoted by late magmatic oxidation of the intrusion.
- Most of the mineralogical and geochemical characteristics that make the Beauvoir granite distinctive result from magmatic rather than hydrothermal processes. However, feldspar and mica compositions and fractionation patterns for some elements (Mn) confirm that post-magmatic fluids were involved in the final stages of crystallization of the intrusion.

ACKNOWLEDGEMENTS

Numerous discussions and field excursions with J. Michaud, A. Villaros, E. Gloaguen have been a constant source of motivation. E. Gloaguen also provided references of mineralogical data on the Beauvoir granite. M. Harlaux shared his expertise on Beauvoir and L. Monnier provided unpublished data. Ida Di Carlo and S. Erdmann helped with the analytical characterization of experimental charges. At Nancy, discussions with B. Charoy, C. Marignac and M. Cuney were particularly helpful and inspiring. The experiments were performed together with M. Aïssa. This paper benefited from reviews on an early draft by C. Marignac and L. Raimbault and from official reviews by M. Cuney, E. Christiansen and X.L. Xiong, as well as from editorial work by A. Audétat.

FUNDING

Recent work on the Beauvoir granite at Orléans was supported by the LABEX VOLTAIRE, the ERAMIN project NewOres and the ANR project VARPEG.

SUPPLEMENTARY DATA

Supplementary data for this paper are available at Journal of Petrology online.

REFERENCES

Ackerson, M.A., Mysen, B.O., Tailby, N.D. & Watson, E.B. (2018). Low-temperature crystallization of granites and the implications for crustal magmatism. *Nature*, doi.org/10.1038/s41586-018-0264-2.

Aïssa, M., Weisbrod, A. & Marignac, C. (1987). Caractéristiques chimiques et thermodynamiques des circulations hydrothermales du site d'Echassières. *Géologie de la France* **2-3**, 335-350.

Aksyuk, A.M., Konyshev, A.A., Korzhinskayaa, V.S. & Shapovalova, Yu.B. (2016). Experimental study of physical and chemical melting conditions of rare-metal granites at the Voznesenka ore cluster, Primorye Region. *Doklady Earth Sciences* **470**, 921–923.

Albarède, F. (1995). *Introduction to geochemical modelling*. Cambridge University Press, 543 p.

Aubert, G. (1969). *Les coupoles granitiques de Montebras et d'Echassières (Massif central français) et la génèse de leurs minéralisations en étain, lithium, tungstène et béryllium*. Mémoire BRGM 46, 345 p.

Audétat, A., Garbe-Schönberg, D., Kronz, A., Pettke, T., Rusk, B., Donovan, J.J. & Lowers, H.A. (2014). Characterisation of a natural quartz crystal as a reference material for microanalytical determination of Ti, Al, Li, Fe, Mn, Ga and Ge. *Geostandards and Geoanalytical Research* **39**, 171-184.

Augier, R., Choulet, F., Faure, M. & Turrillot, P. (2015). A turning-point in the evolution of the Variscan orogen: the ca. 325 Ma regional partial-melting event of the coastal South Armorican domain (South Brittany and Vendée, France). *Bulletin de la Société Géologique de France* **186**, 63-91.

Barbey, P., Villaros, A., Marignac, C. & Montel, J.-M. (2015). Multiphase melting, magma emplacement and P-T-time path in late-collisional context: the Velay example (Massif Central, France). *Bulletin de la Société Géologique de France* **186**, 93-116.

Bénard, F., Moutou, P. & Pichavant, M. (1985). Phase relations of tourmaline leucogranites and the significance of tourmaline in silicic magmas. *Journal of Geology* **93**, 271-291.

Bhalla, P., Holtz, F., Linnen, R.L. & Behrens, H. (2005). Solubility of cassiterite in evolved granitic melts: effect of T, fO2, and additional volatiles. *Lithos* **80**, 387-400.

Breiter, K. (2012). Nearly contemporaneous evolution of the A- and S-type fractionated granites in the Krušné hory/Erzgebirge Mts., Central Europe. *Lithos* **151**, 105–121.

Breiter, K., Fryda, J., Seltmann, R. & Thomas, R. (1997). Mineralogical evidence for two magmatic stages in the evolution of an extremely fractionated P-rich rare-metal granite: the Podlesı stock, Krusne Hory, Czech Republic. *Journal of Petrology* **38**, 1723-1739.

Breiter et al. (2014). Trace element composition of quartz from different types of pegmatites: A case study from the Moldanubian Zone of the Bohemian Massif (Czech Republic). *Mineralogical Magazine* **78**, 703-722.

Burnham, C.W. & Nekvasil, H. (1986). Equilibrium properties of granite pegmatite magmas. *American Mineralogist* **71**, 239-263.

Cerny, P., Blevin, P.L., Cuney, M. & London, D. (2005a). Granite-related ore deposits. *Economic Geology 100th Anniversary Volume*, 337-370.

Cerny, P., Masau, M., Goad, B.E. & Ferreira, K. (2005b). The Greer Lake leucogranite, Manitoba, and the origin of lepidolite-subtype granitic pegmatites. *Lithos* **80**, 305-321.

Charoy, B., Chaussidon, M., Le Carlier de Veslud, C. & Duthou, J.-L. (2003). Evidence of Sr mobility in and around the albite–lepidolite–topaz granite of Beauvoir (France): an in-situ ion and electron probe study of secondary Sr-rich phosphates. *Contributions to Mineralogy and Petrology* **145**, 673-690.

Christiansen, E.H., Sheridan, M.F. & Burt, D.M. (1986). The geology and geochemistry of Cenozoic topaz rhyolite from the western United States. *Geological Society of America Special Paper* **205**, 1–82.

Costi, H.T., Dall'Agnol, R., Pichavant, M. & Rämö, O.T. (2009). The peralkaline tin-mineralized Madeira cryolite albite-rich granite of Pitinga, Amazonian craton, Brasil: petrography, mineralogy and crystallization processes. *Canadian Mineralogist* **47**, 1301-1327.

Cuney, M. & Autran, A. (1987). Objectifs généraux du projet GPF Echassières n°1 et résultats essentiels acquis par le forage de 900 m sur le granite albitique à topaze-lépidolite de Beauvoir. *Géologie de la France* **2-3**, 7-24.

Cuney, M. & Marignac, C. (2015). Rare metal, W and U deposits and related granites from the NE French Massif Central. Field Guide for the 13th Biennial SGA Meeting, 155 p.

Cuney, M., Marignac, C. & Weisbrod, A. (1992). The Beauvoir topaz-lepidolite albite granite (Massif Central, France): The disseminated magmatic Sn-Li-Ta-Nb-Be mineralization. *Economic Geology* **87**, 1766-1794.

Cuney, M. & Barbey, P. (2014). Uranium, rare metals, and granulite-facies metamorphism. *Geoscience Frontiers* **5**, 729-745.

Debon, F. & Le Fort, P. (1983). A chemical-mineralogical classification of common plutonic rocks and associations. Transactions of the Royal Society of Edinburgh, Earth Sciences **73**, 135-149.

Eugster, H.P. (1957). Heterogeneous reactions involving oxidation and reduction at high pressures and temperatures. *Journal of Chemical Physics* **26**, 1760–1761.

Faure, M., Lardeaux, J.-M. & Ledru, P. (2009). A review of the pre-Permian geology of the Variscan French Massif Central. *Comptes Rendus Geosciences* **341**, 202–213.

Fouillac, A. M. & Rossi, P. (1991). Near-solidus ^{18}O depletion in a Ta-Nb-bearing albite granite: the Beauvoir Granite, France. *Economic Geology* **86**, 1704-1720.

French, B.M., Jezek, P.A. & Appleman, D.E. (1978). Virgilite: a new lithium aluminum silicate mineral from the Macusani glass, Peru. *American Mineralogist* **63**, 461-465.

Gardien, V., Lardeaux, J.-M., Ledru, P., Allemand, P. & Guillot, S. (1997). Metamorphism during late-orogenic extension: insights from the French Variscan belt. *Bulletin de la Société Géologique de France*, **168**, 271-286.

Gebelin, A., Roger, F. & Brunel, M. (2009). Syntectonic crustal melting and high-grade metamorphism in a transpressional regime, Variscan Massif Central, France. *Tectonophysics* **477**, 229–243

Glazner, A.F. & Johnson, B.R. (2013). Late crystallization of K-feldspar and the paradox of megacrystic granites. *Contributions to Mineralogy and Petrology* **166**, 777-799.

Hanson, G.N. (1978). The application of trace elements to the petrogenesis of igneous rocks of granitic composition. *Earth and Planetary Science Letters* **38**, 26–43.

Harlaux, M., Mercadier, J., Bonzi, W.M.-E., Kremer, V., Marignac, C. & Cuney, M. (2017). Geochemical signature of magmatic-hydrothermal fluids exsolved from the Beauvoir rare-metal granite (Massif Central, France): Insights from LA-ICPMS analysis of primary fluid inclusions. *Geofluids* 1925817, doi.org/10.1155/2017/1925817.

Harlaux, M., Romer, R.L., Mercadier, J., Morlot, C., Marignac, C. & Cuney, M. (2018). 40 Ma of hydrothermal W mineralization during the Variscan orogenic evolution of the French Massif Central revealed by U-Pb dating of wolframite. *Mineralium Deposita* **53**, 21-51.

Holtz, F., Johannes, W. & Pichavant, M. (1992a). Effect of excess aluminium on phase relations in the system Qz-Ab-Or: experimental investigation at 2 kbar and reduced H2O activity. *European Journal of Mineralogy* **4**, 137-152.

Holtz, F., Johannes, W. & Pichavant, M. (1992a). Peraluminous granitoids: the effect of alumina on melt composition and coexisting minerals. *Transactions of the Royal Society of Edinburgh: Earth Sciences* **83**, 409-416.

Holtz, F., Dingwell, D.B. & Behrens, H. (1993). Effects of F, B2O3 and P2O5 on the solubility of water in haplogranite melts compared to natural silicate melts. *Contributions to Mineralogy and Petrology* **113**, 492-501.

Huang, F., Scaillet, B., Wang, R., Erdmann, S., Chen, Y., Faure, M., Liu, H., Xie, L., Wang, B. & Zhu, J. (2021). Experimental constraints on intensive crystallization parameters and fractionation in A-type granites: A case study on the Qitianling pluton, South China. Journal of Geophysical Research Solid Earth **124**, doi.org/10.1029/2019JB017490.

Hulsbosch, N. (2019). Nb-Ta-Sn-W distribution in granite-related ore systems: fractionation mechanisms and examples from the Karagwe-Ankole belt of Central Africa. In *Ore Deposits, Origin, Exploitation, and Exploitation*, AGU Geophysical Monograph Series, 75-107.

Icenhower, J. & London, D. (1995). An experimental study of element partitioning among biotite, muscovite and coexisting peraluminous silicic melt at 200 MPa (H2O). *American Mineralogist* 80, 1229–1251.

Icenhower, J.P. & London, D. (1997). Partitioning of fluorine and chlorine between biotite and granitic melt: experimental calibration at 200 MPa H2O. *Contributions to Mineralogy and Petrology* **127**, 17–29.

Johan, V., Monier, G. & Rossi, P. (1988). *Etude pétrographique systématique des granites du sondage GPF1 de Beauvoir*. Doc BRGM 124, 91 p.

Kontak, D.J, Clark, A.H. & Farrar E. (1984). The influences of fluid and rock compositions, and tectono-thermal processes on Al-Si distribution in alkali feldspars in granitoid rocks, S.E. Peru. *Bulletin de Minéralogie* **107**, 387-400.

Kosakevitch, A. (1976). *Evolution de la minéralisation en Li, Ta et Nb dans la coupole granitique de Beauvoir (massif d'Echassières, Allier).* Document BRGM, 205 p.

Kovalenko, V.I. (1979). *Experimental studies on the conditions of formation of rare metal-, Li-, F-rich granites*. Nauka, Moscow, 150 p.

Kovalenko, V.I., Tsareva, G.M. & Cuney, M. (1998). Major-, trace elements and water in the magma of the Beauvoir rare metal granite, France (melt inclusion data). *Doklady Akademii Nauk* **358**, 667–671.

Lahlafi, M. (1997). *Rôle des micas dans la concentration des éléments légers (Li, Be et F) dans les granites crustaux: étude expérimentale et cristallochimique*. Thèse de Doctorat, Université d'Orléans, 362 p.

Lardeaux, J.-M. (2014). Deciphering orogeny: a metamorphic perspective. Examples from European Alpine and Variscan belts. Part II: Variscan metamorphism in the French Massif Central - a review. *Bulletin de la Société Géologique de France* **185**, 281–310.

La Roche, H. de, Stussi, J.-M. & Chauris, L. (1980). Les granites à deux micas hercyniens français. Essai de cartographies et de corrélations géochimiques appuyées sur une banque de données. Implications pétrologiques et métallogéniques. *Sciences de la Terre, Nancy* **XXIV**, 5-121.

Linnen, R.L. (1998). The solubility of Nb-Ta-Zr-Hf-W in granitic melts with Li and Li + F: constraints for mineralization in rare metal granites and pegmatites. *Economic Geology* **93**, 1913-1925.

Linnen, R.L. & Keppler, H. (1997). Columbite solubility in granitic melts: consequences for the enrichment and fractionation of Nb and Ta in the Earth's crust. *Contributions to Mineralogy and Petrology* **128**, 213-227.

Linnen, R.L. & Cuney, M. (2005). Granite-related rare-element deposits and experimental constraints on Ta-Nb-W-Sn-Zr-Hf mineralization. In: Linnen RL and Samson IM (eds) *Rare-element geochemistry and mineral deposits*, Geological Association of Canada, **17**, 45-68.

Linnen, R.L., Pichavant, M., Holtz, F. & Burgess, S. (1995). The effect of fO2 on the solubility, diffusion and speciation of tin in haplogranitic melt at 850°C and 2 kbar. *Geochimica et Cosmochimica Acta* **59**, 1579-1588.

Linnen, R.L., Pichavant, M. & Holtz, F. (1996). The combined effect of fO2 and melt composition on SnO2 solubility and tin diffusivity in haplogranitic melts. *Geochimica et Cosmochimica Acta*, **60**, 4965-4976.

London, D. (1992). Phosphorus in S-type magmas: the P2O5 content of feldspars from peraluminous granites, pegmatites, and rhyolites. *American Mineralogist* **77**, 126-145.

London, D. (2008). *Pegmatites*. Canadian Mineralogist Special Publication **10**, 368 p.

London, D., Morgan, G.B.VI & Hervig, R.L. (1989). Vapor-undersaturated experiments with Macusani glass+ H20 at 200 MPa, and the internal differentiation of granitic pegmatites. *Contributions to Mineralogy and Petrology* **102**, 1-17.

London, D., Morgan, G.B., VI, Babb, H.A. & Loomis, J.L. (1993). Behavior and effects of phosphorus in the system Na2O–K2O–Al2O3–SiO2–P2O5–H2O at 200 MPa (H2O). *Contributions to Mineralogy and Petrology* **113**, 450–465.

London, D., Wolf, M.B., Morgan, G.VI & Gallego Garrido, M. (1999). Experimental silicate–phosphate equilibria in peraluminous granitic magmas, with a case study of the Alburquerque batholith at Tres Arroyos, Badajoz, Spain. *Journal of Petrology* **40**, 215-240.

London, D., Morgan, G.VI & Wolf, M.B. (2001). Amblygonite-montebrasite solid solutions as monitors of fluorine in evolved granitic and pegmatitic melts. *American Mineralogist* **86**, 225-233.

London, D., Hunt, L.E., Schwing, C.R. & Guttery, B.M. (2020). Feldspar thermometry in pegmatites: truth and consequences. *Contributions to Mineralogy and Petrology* **175**, 8, doi-org.insu.bib.cnrs.fr/10.1007/s00410-019-1617-z.

Lukkari, S. & Holtz, F. (2007). Phase relations of a F-enriched peraluminous granite: an experimental study of the Kymi topaz granite stock, southern Finland. Contributions to Mineralogy and Petrology **153**, 273–288.

Luth, W.C. (1976). *Granitic rocks*. In: Bailey, D.K., MacDonald, R. (Eds.), The Evolution of Crystalline Rocks. Academic Press, London, 335-417.

Manning, D.A.C. (1981). The effect of fluorine on liquidus phase relationships in the system Qz-Ab-Or with excess water at 1 kbar. *Contributions to Mineralogy and Petrology* **76**, 206-215.

Marcoux, E., Barré, B., Pichavant, M. & Poujol, M. (2021). Âge et genèse de la coupole granitique à métaux rares (Sn, Li, Nb-Ta, W) de Montebras (Creuse, Massif central français). *BSGF – Earth Science Bulletin* **192**, 16.

Marignac, C., Cuney, M., Kesraoui, M. & Bouabsa, L. (2009). Differentiation-dedifferentiation processes in the rare metal granite (RMG) lineages. Proceedings of the 10th biennal SGA meeting, Townsville, EGRU, 991-993.

Martin, J.S. (1983). An experimental study of the effect of lithium on the granite system. *Proceedings of the Ussher Society* **5**, 417-420.

Michaud, J.A.-S. & Pichavant, M. (2020). Magmatic fractionation and the magmatic-hydrothermal transition in rare metal granites: evidence from Argemela (Central Portugal). *Geochimica et Cosmochimica Acta* **289**, 130-157.

Michaud, J.A.-S., Pichavant, M. & Villaros, A. (2021). Rare elements enrichment in crustal peraluminous magmas: insights from partial melting experiments. *Contributions to Mineralogy and Petrology* **176**, 96, doi.org/10.1007/s00410-021-01855-9.

Moazzen, M. & Droop, G.T.R. (2005). Application of mineral thermometers and barometers to granitoid igneous rocks: the Etive Complex, W Scotland. *Mineralogy and Petrology* **83**, 27-53.

Monier, G. & Tegyey, M. (1985). *Etude pétrographique préliminaire du sondage "GPF Echassières I"*. Doc. BRGM n° 100, 41-93.

Monier, G., Charoy, B., Cuney, M., Ohnenstetter, D. & Robert, J.-L. (1987). Evolution spatiale et temporelle de la composition des micas du granite albitique à topaze-lépidolite de Beauvoir. *Géologie de la France* **2-3**, 179-188.

Monnier, L., Salvi, S., Melleton, J., Bailly, L., Béziat, D., de Parseval, P., Gouy, S. & Lach, P. (2019). Multiple Generations of wolframite mineralization in the Echassières district (Massif Central, France). *Minerals* **9**, 637, doi:10.3390/min9100637.

Monnier, L., Salvi, S., Jourdan, V., Salla, S., Bailly, L., Melleton, J. & Béziat, D. (2020). Contrasting fluid behavior during two styles of greisen alteration leading to distinct wolframite mineralizations: The Echassières district (Massif Central, France). *Ore Geology Reviews* **124**, 103648.

Muller, A., Romer, R. & Pedersen, R.-B. (2017). The Sveconorwegian pegmatite province - thousands of pegmatites without parental granites. *Canadian Mineralogist* **55**, 283–315.

Nabelek, P.I., Russ-Nabelek, C. & Denison, J.R. (1992a). The generation and crystallization conditions of the Proterozoic Harney Peak Leucogranite, Black Hills, South Dakota, USA: Petrologic and geochemical constraints. *Contributions to Mineralogy and Petrology* **110**, 173-191.

Nabelek, P.I., Russ-Nabelek, C. & Haeussler, G.T. (1992b). Stable isotope evidence for the petrogenesis and fluid evolution in the Proterozoic Harney Peak leucogranite, Black Hills, South Dakota. *Geochimica et Cosmochimica Acta* **56**, 403-417.

Nekvasil, H. & Burnham, C.W. (1987). The calculated individual effects of pressure and water content on phase equilibria in the granite system. In *Magmatic Processes: Physicochemical Principles*. The Geochemical Society, Special Publication **1**, 433–445.

Neukampf, J., Ellis, B., Magna, T., Laurent, O. & Bachmann, O. (2019). Partitioning and isotopic fractionation of lithium in mineral phases of hot, dry rhyolites: the case of the Mesa Falls Tuff, Yellowstone. *Chemical Geology* **506**, 175–186.

Parsons, I. (1978). Feldspars and fluids in cooling plutons. *Mineralogical Magazine* 42, 1-17.

Pearce, N.J.G., Perkins, W.T., Westgate, J.A., Gorton, M.P., Jackson, S.E., Neal, C.R., Chenery, S.P. (1997). A compilation of new and published major and trace element data for NIST SRM 610 and NIST SRM 612 glass reference materials. *Geostandard Newsletter* **21**, 115–144.

Pichavant, M. (1987). Effects of B and H2O on liquidus phase relations in the haplogranite system at 1 kbar. *American Mineralogist* **72**, 1056–1070.

Pichavant, M., Boher, M., Stenger, J.-F., Aïssa, M. & Charoy, B. (1987a). Relations de phases des granites de Beauvoir entre 1 et 3 kbar en conditions de saturation en H2O. *Géologie de la France* **2–3**, 77–86.

Pichavant, M., Valencia Herrera, J., Boulmier, S., Briqueu, L., Joron, J.-L., Juteau, M., Michard, A., Sheppard, S.M.F., Treuil, M. & Vernet, M. (1987b). The Macusani glasses, SE Peru: evidence of chemical fractionation in peraluminous magmas. In *Magmatic Processes: Physicochemical Principles*. The Geochemical Society, Special Publication **1**, 359–373.

Pichavant, M., Villaros, A., Deveaud, S., Scaillet, B. & Lahlafi, M. (2016). The influence of redox state on mica crystallization in leucogranitic and pegmatitic liquids. *Canadian Mineralogist* **54**, 559-581.

Piwinskii, A.J. & Martin, R.F. (1970). An experimental study of equilibrium with granitic rocks at 10 kbar. *Contributions to Mineralogy and Petrology* **29**, 1-10.

Pollard P. J. (2021). The Yichun Ta-Sn-Li deposit, South China: Evidence for extreme chemical fractionation in F-Li-P-Rich magma. *Economic Geology* **116**, 453-469.

Raimbault, L. (1998). Composition of complex lepidolite-type granitic pegmatites and of constituent columbite-tantalite, Chédeville, Massif Central, France. *Canadian Mineralogist* **36**, 563–583.

Raimbault, L. & Burnol, L. (1998). The Richemont rhyolite dyke, Massif Central, France: a subvolcanic equivalent of rare metal granites. *Canadian Mineralogist* **36**, 265-282.

Raimbault, L., Cuney, M., Azencott, C., Duthou, J.-L. & Joron, J.-L. (1995). Geochemical evidence for a multistage magmatic genesis of Ta-Sn-Li mineralization in the granite at Beauvoir, French Massif Central. *Economic Geology* **90**, 548-576.

Roda-Robles, E., Pesquera, A., Gil-Crespo, P.P., Vieira, R., Lima, A., Garate-Olave, I., Martins, T. & Torres-Ruiz, J. (2016). Geology and mineralogy of Li mineralization in the Central Iberian Zone (Spain and Portugal). *Mineralogical Magazine* **80**, 103-126.

Roda-Robles, E., Villaseca, C., Pesquera, A., Gil-Crespo, P.P., Vieira, R., Lima, A. & Garate-Olave, I. (2018). Petrogenetic relationships between Variscan granitoids and Li-(F-P)-

rich aplite-pegmatites in the Central Iberian Zone: geological and geochemical constraints and implications for other regions from the European Variscides. *Ore Geology Reviews* **95**, 408-430.

Romer, R.L. & Pichavant, M. (2021). Rare metal granites and pegmatites. In: Alderton, D., Elias, S.A. (eds.), *Encyclopedia of Geology*, 2nd edition., **5**, 840-846.

Rossi, P., Autran, A., Azencott, C., Burnol, L., Cuney, M., Johan, V. & Raimbault, L. (1987). Logs pétrographiques et géochimiques du granite de Beauvoir dans le sondage GPF "Echassières I": minéralogie et géochimie comparée. *Géologie de la France* **2-3**, 111–135.

Scaillet, B., Pichavant, M. & Roux, J. (1995). Experimental crystallization of leucogranite magmas. *Journal of Petrology* **36**, 663–705.

Schmidt, B., Scaillet, B. & Holtz, F. (1995). Accurate control of fH(2) in cold-seal pressure vessels with the Shaw membrane technique. *European Journal of Mineralogy* **7**, 893–903.

Simpson, D.R. (1977). Aluminum phosphate variants of feldspar. *American Mineralogist* **62**, 351-355.

Sirbescu, M.-L., Schmidt, C., Veksler, I.V., Whittington, A.G. & Wilke, M. (2017). Experimental crystallization of undercooled felsic liquids: generation of pegmatitic texture. *Journal of Petrology* **58**, 539-568.

Smith, J.V. & Brown, W.L. (1988). *Feldspar minerals. Volume 1 Crystal Structures, Physical, Chemical, and Microtextural Properties*. Springer, 828 p.

Stewart, D.B. (1978). Petrogenesis of lithium-rich pegmatites. *American Mineralogist* **63**, 970-980.

Soufi, M. (2021). Origin and physical-chemical control of topaz crystallization in felsic igneous rocks: Contrasted effect of temperature on its OH–F substitution. *Earth Science Reviews* **213**, 103467.

Taylor, H.P.Jr. & Forester, R.W. (1971). Low-O18 igneous rocks from the intrusive complexes of Skye, Mull, and Ardnamurchan, Western Scotland. *Journal of Petrology* **12**, 465-497.

Tischendorf, G., Gottesmann, B., Förster, H.-J. & Trumbull, R.B. (1997). On Li-bearing micas: estimating Li from electron microprobe analyses and an improved diagram for graphical representation. *Mineralogical Magazine* **61**, 809–834.

Tuttle, O.F., Bowen, N.L. (1958). Origin of granite in the light of experimental studies in the system NaAlSi3O8-KAlSi3O8-SiO2-H2O. *Geological Society of America Memoir* 74, 153 p.

Xiong, X.L., Zhao, Z.H., Zhu, J.C., Rao, B. & Lai, M.Y. (1998). Phase equilibria in the granite-H2O-HF system and effect of fluorine on granitic melt structure. *Chinese Journal of Geochemistry* **17**, 114-122.

Xiong, X.L., Zhao, Z.H., Zhu, J.C. & Rao, B. (1999). Phase relations in albite granite-H2O-HF system and their petrogenetic applications. *Geochemical Journal* **33**, 199-214.

Xiong, X.L., Rao, B., Chena, F.R., Zhu, J.C. & Zhao, Z.H. (2002). Crystallization and melting experiments of a fluorine-rich leucogranite from the Xianghualing Pluton, South China, at 150 MPa and H2O-saturated conditions. *Journal of Asian Earth Sciences* **21**, 175-188.

Van Lichtervelde, M., Holtz, F. & Melcher, F. (2018). The effect of disequilibrium crystallization on Nb-Ta fractionation in pegmatites: Constraints from crystallization experiments of tantalite-tapiolite. *American Mineralogist* **103**, 1401-1416.

Villaros, A., Pichavant, M. & Deveaud, S. (2019). Mica-liquid trace elements partitioning and the granite-pegmatite connection: The St-Sylvestre complex (Western French Massif Central). *Chemical Geology* **528**, 119265.

Weidner, J.R. & Martin, R.F. (1987). Phase equilibria of a fluorine-rich leucogranite from the St. Austell pluton, Cornwall. *Geochimica et Cosmochimica Acta* **51**, 1591-1597.

Wen, S. & Nekvasil, H. (1994). SOLVALC: an interactive graphics program package for calculating the ternary feldspar solvus and for two feldspar geothermometry. *Computers and Geosciences* **20**, 1025e1040.

Zhu, J.C., Li, R.K., Li, F.C., Xiong, X.L., Zhou, F.Y. & Huang, X.L. (2001). Topaz albite granites and rare-metal mineralization in the Limu district, Guangxi provine, southeast China. *Mineralium Deposita* **36**, 393-405.

FIGURE CAPTIONS

Fig. 1. SEM images of major phases and textures in crystallization experiments. (a) euhedral quartz (Qz) and plagioclase (Pl) in glass (Gl), charge B2N-18. (b) large homogenenous plagioclase crystals (Pl) in glass (Gl), charge B1N-1. (c) large heterogeneous feldspar crystals in glass (Gl), charge B2N-3. The potassic and sodic zones are denoted by K and Na respectively. Notice the progressive and geometrically complex transitions between the two zones and the small quartz (Qz) crystals at the extremities of the feldspars. (d) euhedral homogeneous K-feldspar crystals (Af) coexisting with homogeneous plagioclase (Pl) in

composite crystals embedded in glass (Gl), charge B1N-22. (e) Li-mica crystals (Li-Mi) in glass (Gl), charge B2N-25. Apatite (Ap) appears in white at the bottom of the image. (f) Euhedral topaz crystals (Tpz) coexisting with quartz (Qz), K-feldspar (Af), plagioclase (Pl), Li-mica (small white grey interstitial phases and aggregates) and glass (Gl) in charge B1-21. (g) Several crystals of Li-Al phosphates (LiP) of the amblygonite-montebrasite series dispersed in charge B1-21. Notice also the presence of topaz (Tpz). (h) Crystal of hematite (Hm) in glass (Gl), charge B2N-19. See Tables 2 and 3 for experimental conditions.

Fig. 2. Summary P-T phase diagram for the B1 Beauvoir composition under H_2O-saturated conditions and for a fO_2 between NNO+3 and NNO+1. The solid symbols are experimental data points from Table 2. Solid curves represent phase equilibria constrained from crystallization experiments (this study) and dashed curves from melting experiments (Pichavant et al., 1987a). Solidus curves appear in black and Qz, Pl, Af and Li-Mi saturation curves in red, blue, green and yellow respectively. Phases are stable on the left of their respective saturation curve. The P-T location of minimum liquidus temperature points in the H_2O-saturated haplogranite system ("haplogranite minimum", Tuttle and Bowen, 1958) is shown for comparison (grey solid curve). See text for the construction of the diagram and for interpretations.

Fig. 3. Summary P-T phase diagram for the B2 Beauvoir composition under H_2O-saturated conditions and for a fO_2 between NNO+3 and NNO-1. The solid symbols are experimental data points from Table 3. Solid curves represent phase equilibria constrained from crystallization experiments (this study) and dashed curves from melting experiments (Pichavant et al., 1987a). Solidus curves appear in black and Qz, Pl, Af and Li-Mi saturation curves in red, blue, green and yellow respectively. Phases are stable on the left of their respective saturation curve. The P-T location of minimum liquidus temperature points in the H_2O-saturated haplogranite system ("haplogranite minimum", Tuttle and Bowen, 1958) is shown for comparison (grey solid curve). See text for the construction of the diagram and for interpretations.

Fig. 4. Changes in Beauvoir experimental melt compositions during progressive crystallization and decreasing melt fraction (expressed in wt%). Symbols are in red for B1 and in blue for B2. Melt fractions are melt (L) proportions in experimental charges (solid symbols) calculated by mass balance (Table 2 and 3). For starting melts (open symbols), melt

fractions are 100%. (a) F concentrations (wt%) vs. melt fraction; (b) P_2O_5 concentrations (wt%) vs. melt fraction; (c) normative Corundum (%) vs. melt fraction; (d) normative Anorthite (%) vs. melt fraction. In (a), numbers in grey refer to the charge numbering in Tables 2 and 3. Data for experimental melts are from Table 4 and for starting melts from Table 1. Note that the F and P_2O_5 concentrations are not normalized to 100% anhydrous. Error bars are shown.

Fig. 5. Qz, Ab, Or compositions of Beauvoir starting materials (stars) and experimental glasses (open circles). Symbols are in red for the B1 and in blue for the B2 composition. Normative compositions (data in Tables 1 and 4) are projected on the Qz-Ab-Or space. Numbers in grey refer to the charge numbering in Tables 2 and 3. Note that, in panel B1, compositions of glass B1O-1 and of starting materials overlap and, in panel B2, compositions of glasses B2N-19, B2N-20, B2N-25, B2N-26 and of starting materials overlap. For reference, the positions of H_2O-saturated minimum liquidus temperature points in the haplogranite system at 100, 200 and 300 MPa (Tuttle and Bowen, 1958) are shown as black squares. The positions of H_2O-saturated minimum liquidus temperature points in the haplogranite system at 100 MPa with 1 and 2 wt% added F (Manning, 1981) are shown as black circles.

Fig. 6. Compositions of feldspars in the crystallization experiments. All data from Table S2 are plotted. The B1 symbols and tie-lines are in red and the B2 in blue. Pl: plagioclase; Af: K-feldspar; I: heterogeneous feldspar. Notice the heterogeneous feldspars plotting intermediate between Pl and Af. Two-feldspar equilibration temperatures calculated using the SOLVCALC software of Wen and Nekvasil (1994) for 4 representative Pl and Af pairs are shown together with experimental pressures on their respective tie-lines. For charge B2N-24, the calculated temperature is 578°C (vs. 580°C, Table 3) and, for charge B1N-21, 567°C (vs. 580°C, Table 2). For charge B2N-20, two plagioclase compositions have been selected for the calculations, the < 2 mol% An difference between the two being representative of the chemical dispersion within charges. The two Pl-Af pairs yield temperatures of 608 and 588°C (vs. 620°C, Table 3). Results of other two-feldspar calculations are summarized in text. Average compositions of feldspars in B1 and B2 starting rocks (data from Pichavant et al., 1987a) are shown for comparison.

Fig. 7. Compositions of (a) experimental and (b) natural micas plotted in the $Fe_t + Mn + Ti - Al^{VI}$ (apfu) vs. Mg – Li (apfu) diagram of Tischendorf et al. (1997). Abbreviated names of end-member compositions appear in grey (nomenclature after Tischendorf et al., 1997). Data for experimental micas include electron microprobe (EMPA) and SEM analyses (Table 7 and S3). For the SEM analyses, F concentrations are corrected by a constant factor (x 2.3). The data for the natural Beauvoir micas (Monier et al., 1987) include electron microprobe (EMPA) and wet chemical analyses (CHEM). The data for the natural Argemela micas are averages of EMPA analyses from Michaud and Pichavant (2020). Except for the wet chemical analyses of Beauvoir micas, the Li_2O contents of micas analyzed by EMPA and SEM are all calculated from their F concentrations, using the [di 1] equation of Tischendorf et al. (1997). In (a), 21, 22, 23 refer to the charge number in Table 2. The two arrows represent the evolutionary trends (1) and (2) discussed in text.

Fig. 8. (a) Mg – Li (apfu) and (b) $Fe_t + Mn + Ti - Al^{VI}$ (apfu) of experimental micas as a function of the F content of the coexisting melt. Data for experimental micas include electron microprobe (EMPA) and SEM analyses (Table 7 and S3). For the SEM analyses, F concentrations are corrected by a constant factor (x 2.3). Li_2O concentrations of micas analyzed by EMPA and SEM are all calculated from their F contents, using the [di 1] equation of Tischendorf et al. (1997). F concentrations in experimental melts are raw data from Table 4 (i.e., not normalized to 100%) with error bar shown. 21, 22, 23, 25 refer to the charge number in Table 2 (i.e., 21-23 refers to the B1N-21 to -23 and 25 to the B2N-25 charge). The two arrows represent the evolutionary trends (1) and (2) discussed in text.

Fig. 9. Evolution of trace element concentrations during progressive crystallization of the B2 Beauvoir melt. Concentrations of trace elements (Li, Be, B, Mn, Rb, Cs, W, U, Nb, Ta, Sn, Sr) in selected B2 glasses (C), referenced to those in the initial melt (C_0, represented by the crystal-free charge B2N-26), are plotted as log (C/C_0) vs. the melt fraction (*f*). Glass concentrations are from Table 9 and melt fractions from Table 3. Dashed curves are Rayleigh fractionation trends calculated (see Hanson, 1978) for bulk mineral/melt partition coefficients (D) of 0.01, 0.5 and 3. The horizontal dotted line corresponds to $C = C_0$. See text.

Fig. 10. F concentration in experimental micas as a function of the F content of the coexisting melt. Data for experimental micas include electron microprobe (EMPA) and SEM analyses (Table 7 and S3). F concentrations from SEM data are corrected by a constant factor (x 2.3). F

concentrations in experimental melts are raw data from Table 4 (i.e., not normalized to 100%) with error bar shown. 21, 22, 23, 25 refer to the charge number in Table 2 (i.e., 21-23 refers to the B1N-21 to -23 and 25 to the B2N-25 charge).

Fig. 11. Comparison between major element fractionation in Beauvoir granites (left column) and in experimental glasses from this study (right column). Top panels (a) and (b): major element compositions plotted in the A-B diagram of Debon and Le Fort (1983). Bottom panels (c) and (d): major element compositions plotted in the Q*3-B*3-F*3-M*3 representation of La Roche et al. (1980), see also Cuney and Marignac (2015) and inset for the significance of the Q*3, B*3, F*3, M*3 apexes. Concentrations are expressed in millications, i.e., as 1000 x atomic concentrations (at.). Abbreviations: Qz: quartz, Ann: annite, Phl: phlogopite, Pl: plagioclase, Af: K-feldspar, Mu: muscovite. In (d), experimental mica compositions from charges B1N23 and B2N-25 are also plotted (respectively Li-Mi B1 and Li-Mi B2). The Beauvoir whole rock data are exclusively from Raimbault et al. (1995) and the experimental data are from this paper (averages of starting compositions in Table 1 and selected glass compositions from Table 4). Notice the specific Q*3-rich compositions of glasses B1N-17 and B2N-3 (respectively labelled 17 and 3) from 100 MPa crystallization charges.

Fig. 12. Comparison between trace element (Sn, Ta, Be, Nb, Li, P, U, F, Rb, W, Ti, Mn, Zn, Pb, Sr, Cs) fractionation in experiments from this study and in Beauvoir granites. Horizontal axis: log (C/C_0) where C is the trace element concentration in the most fractionated glass B2-24 and C_0 the trace element concentration in the parental glass B2-26 (Table 9). Vertical axis: log (C/C_0) where C is the trace element concentration in B1 granite (ESP 270, Raimbault et al., 1995) and C_0 the trace element concentration in glass B2-26 (Table 9) assumed representative of the B2 granite. Experimental and natural enrichment and depletion directions are indicated. The location of data points relative to the 1:1 dotted line indicates how close elements are from an evolution identical in experiments and granites, whether an enrichment or a depletion. Color coding reflects the four groups of elements distinguished, those enriched both in the experiments and in the granites (red circles), those depleted both in the experiments and in the granites (black circles), those whose behavior should be controlled by accessory phase solubilities (blue squares) and those very much fractionated neither in the experiments nor in the granite (grey diamonds).

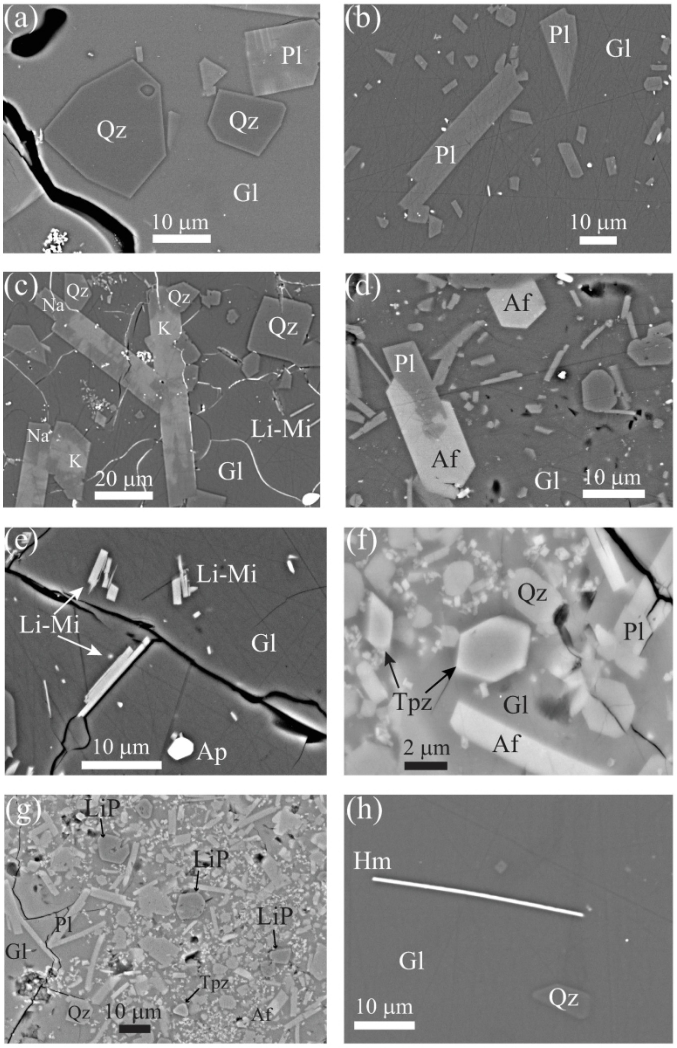

Pichavant, Fig.1

Fig. 1. SEM images of major phases and textures in crystallization experiments. (a) euhedral quartz (Qz) and plagioclase (Pl) in glass (Gl), charge B2N-18. (b) large homogenenous plagioclase crystals (Pl) in glass (Gl), charge B1N-1. (c) large heterogeneous feldspar crystals in glass (Gl), charge B2N-3. The potassic and sodic zones are denoted by K and Na respectively. Notice the progressive and geometrically complex transitions between the two zones and the small quartz (Qz) crystals at the extremities of the feldspars. (d) euhedral homogeneous K-feldspar crystals (Af) coexisting with homogeneous plagioclase (Pl) in composite crystals embedded in glass (Gl), charge B1N-22. (e) Li-mica crystals (Li-Mi) in glass (Gl), charge B2N-25. Apatite (Ap) appears in white at the bottom of the image. (f) Euhedral topaz crystals (Tpz) coexisting with quartz (Qz), K-feldspar (Af), plagioclase (Pl), Li-mica (small white grey interstitial phases and aggregates) and glass (Gl) in charge B1-21. (g) Several crystals of Li-Al phosphates (LiP) of the amblygonite-montebrasite series dispersed in charge B1-21. Notice also the presence of topaz (Tpz). (h) Crystal of hematite (Hm) in glass (Gl), charge B2N-19. See Tables 2 and 3 for experimental conditions.

172x263mm (300 x 300 DPI)

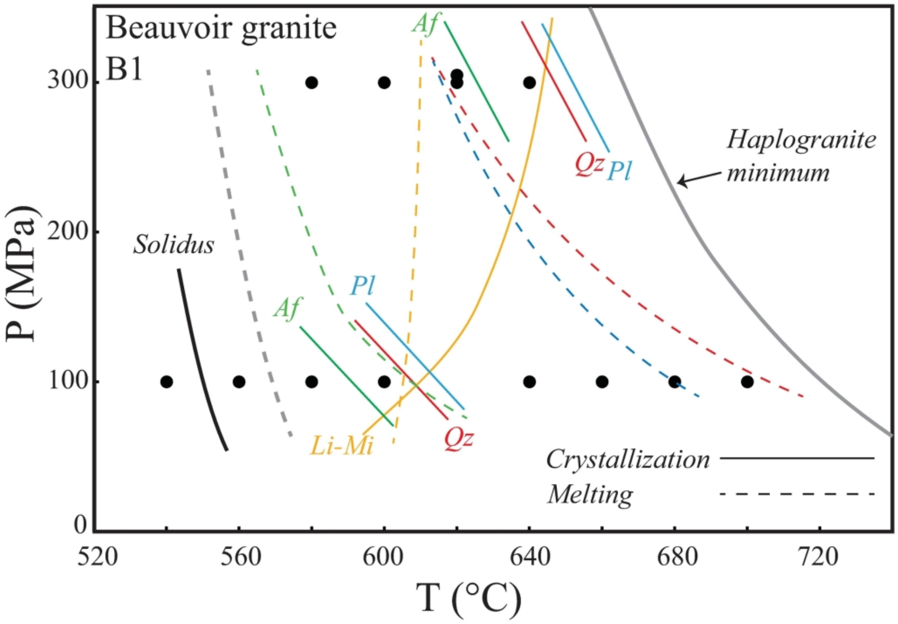

Pichavant, Fig.2

Fig. 2. Summary P-T phase diagram for the B1 Beauvoir composition under H2O-saturated conditions and for a fO2 between NNO+3 and NNO+1. The solid symbols are experimental data points from Table 2. Solid curves represent phase equilibria constrained from crystallization experiments (this study) and dashed curves from melting experiments (Pichavant et al., 1987a). Solidus curves appear in black and Qz, Pl, Af and Li-Mi saturation curves in red, blue, green and yellow respectively. Phases are stable on the left of their respective saturation curve. The P-T location of minimum liquidus temperature points in the H2O-saturated haplogranite system ("haplogranite minimum", Tuttle and Bowen, 1958) is shown for comparison (grey solid curve). See text for the construction of the diagram and for interpretations.

190x244mm (300 x 300 DPI)

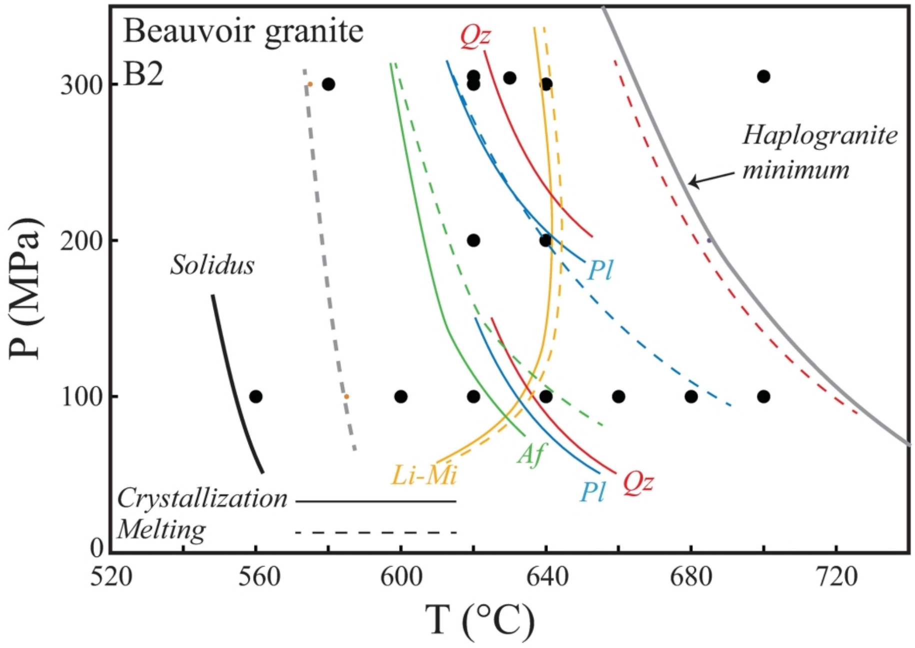

Pichavant, Fig.3

Fig. 3. Summary P-T phase diagram for the B2 Beauvoir composition under H2O-saturated conditions and for a fO2 between NNO+3 and NNO-1. The solid symbols are experimental data points from Table 3. Solid curves represent phase equilibria constrained from crystallization experiments (this study) and dashed curves from melting experiments (Pichavant et al., 1987a). Solidus curves appear in black and Qz, Pl, Af and Li-Mi saturation curves in red, blue, green and yellow respectively. Phases are stable on the left of their respective saturation curve. The P-T location of minimum liquidus temperature points in the H2O-saturated haplogranite system ("haplogranite minimum", Tuttle and Bowen, 1958) is shown for comparison (grey solid curve). See text for the construction of the diagram and for interpretations.

184x234mm (300 x 300 DPI)

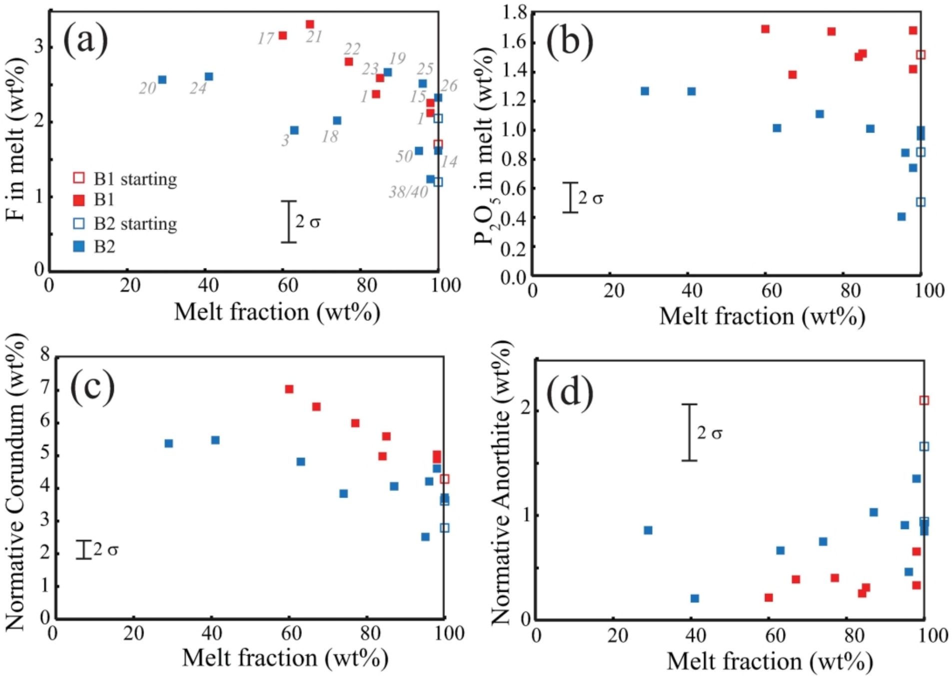

Pichavant, Fig.4

Fig. 4. Changes in Beauvoir experimental melt compositions during progressive crystallization and decreasing melt fraction (expressed in wt%). Symbols are in red for B1 and in blue for B2. Melt fractions are melt (L) proportions in experimental charges (solid symbols) calculated by mass balance (Table 2 and 3). For starting melts (open symbols), melt fractions are 100%. (a) F concentrations (wt%) vs. melt fraction; (b) P2O5 concentrations (wt%) vs. melt fraction; (c) normative Corundum (%) vs. melt fraction; (d) normative Anorthite (%) vs. melt fraction. In (a), numbers in grey refer to the charge numbering in Tables 2 and 3. Data for experimental melts are from Table 4 and for starting melts from Table 1. Note that the F and P2O5 concentrations are not normalized to 100% anhydrous. Error bars are shown.

191x242mm (300 x 300 DPI)

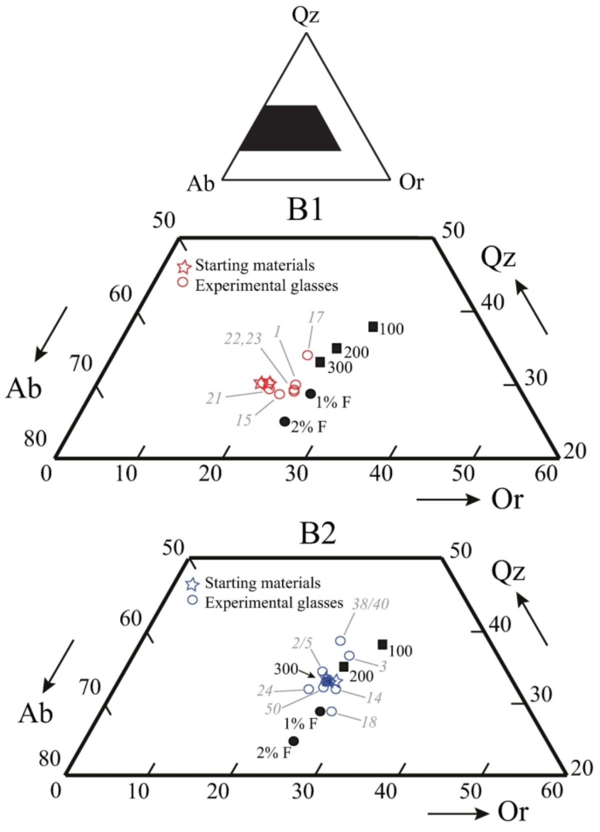

Pichavant, Fig. 5

Fig. 5. Qz, Ab, Or compositions of Beauvoir starting materials (stars) and experimental glasses (open circles). Symbols are in red for the B1 and in blue for the B2 composition. Normative compositions (data in Tables 1 and 4) are projected on the Qz-Ab-Or space. Numbers in grey refer to the charge numbering in Tables 2 and 3. Note that, in panel B1, compositions of glass B1O-1 and of starting materials overlap and, in panel B2, compositions of glasses B2N-19, B2N-20, B2N-25, B2N-26 and of starting materials overlap. For reference, the positions of H2O-saturated minimum liquidus temperature points in the haplogranite system at 100, 200 and 300 MPa (Tuttle and Bowen, 1958) are shown as black squares. The positions of H2O-saturated minimum liquidus temperature points in the haplogranite system at 100 MPa with 1 and 2 wt% added F (Manning, 1981) are shown as black circles.

134x250mm (300 x 300 DPI)

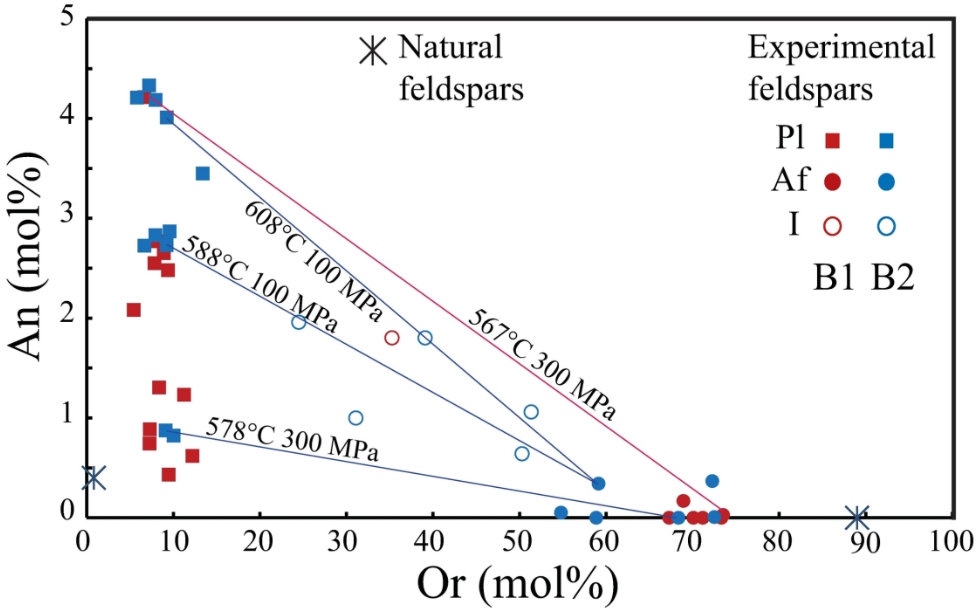

Pichavant, Fig. 6

Fig. 6. Compositions of feldspars in the crystallization experiments. All data from Table S2 are plotted. The B1 symbols and tie-lines are in red and the B2 in blue. Pl: plagioclase; Af: K-feldspar; I: heterogeneous feldspar. Notice the heterogeneous feldspars plotting intermediate between Pl and Af. Two-feldspar equilibration temperatures calculated using the SOLVCALC software of Wen and Nekvasil (1994) for 4 representative Pl and Af pairs are shown together with experimental pressures on their respective tie-lines. For charge B2N-24, the calculated temperature is 578°C (vs. 580°C, Table 3) and, for charge B1N-21, 567°C (vs. 580°C, Table 2). For charge B2N-20, two plagioclase compositions have been selected for the calculations, the < 2 mol% An difference between the two being representative of the chemical dispersion within charges. The two Pl-Af pairs yield temperatures of 608 and 588°C (vs. 620°C, Table 3). Results of other two-feldspar calculations are summarized in text. Average compositions of feldspars in B1 and B2 starting rocks (data from Pichavant et al., 1987a) are shown for comparison.

176x217mm (300 x 300 DPI)

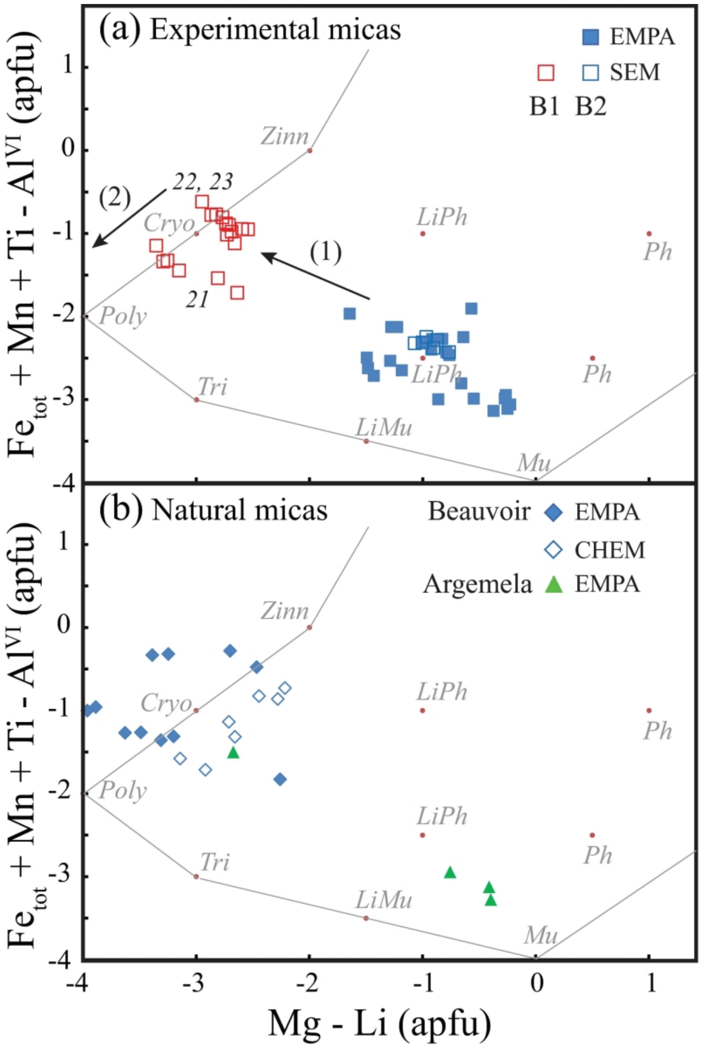

Pichavant, Fig.7

Fig. 7. Compositions of (a) experimental and (b) natural micas plotted in the Fet + Mn + Ti – AlVI (apfu) vs. Mg – Li (apfu) diagram of Tischendorf et al. (1997). Abbreviated names of end-member compositions appear in grey (nomenclature after Tischendorf et al., 1997). Data for experimental micas include electron microprobe (EMPA) and SEM analyses (Table 7 and S3). For the SEM analyses, F concentrations are corrected by a constant factor (x 2.3). The data for the natural Beauvoir micas (Monier et al., 1987) include electron microprobe (EMPA) and wet chemical analyses (CHEM). The data for the natural Argemela micas are averages of EMPA analyses from Michaud and Pichavant (2020). Except for the wet chemical analyses of Beauvoir micas, the Li2O contents of micas analyzed by EMPA and SEM are all calculated from their F concentrations, using the [di 1] equation of Tischendorf et al. (1997). In (a), 21, 22, 23 refer to the charge number in Table 2. The two arrows represent the evolutionary trends (1) and (2) discussed in text.

165x240mm (300 x 300 DPI)

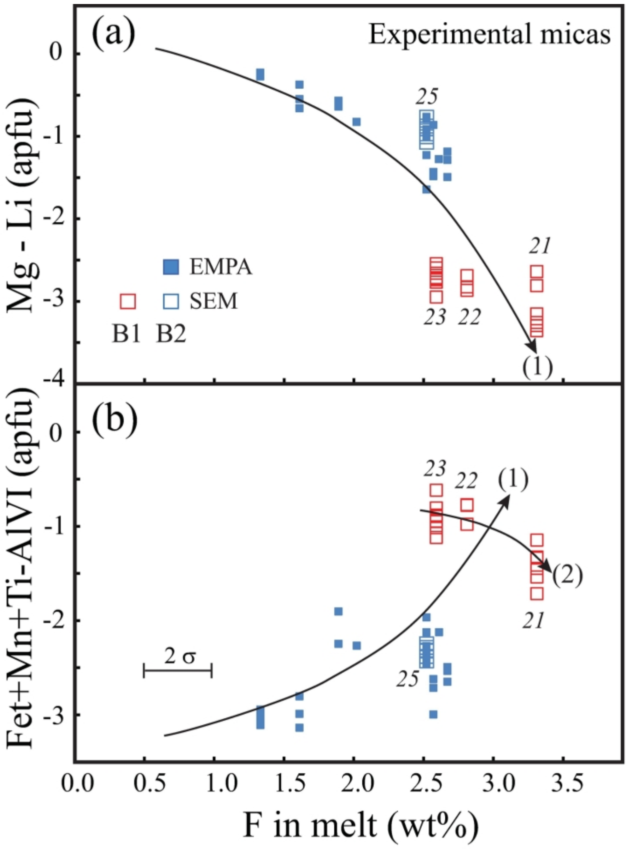

Pichavant, Fig.8

Fig. 8. (a) Mg – Li (apfu) and (b) Fet + Mn + Ti – AlVI (apfu) of experimental micas as a function of the F content of the coexisting melt. Data for experimental micas include electron microprobe (EMPA) and SEM analyses (Table 7 and S3). For the SEM analyses, F concentrations are corrected by a constant factor (x 2.3). Li2O concentrations of micas analyzed by EMPA and SEM are all calculated from their F contents, using the [di 1] equation of Tischendorf et al. (1997). F concentrations in experimental melts are raw data from Table 4 (i.e., not normalized to 100%) with error bar shown. 21, 22, 23, 25 refer to the charge number in Table 2 (i.e., 21-23 refers to the B1N-21 to -23 and 25 to the B2N-25 charge). The two arrows represent the evolutionary trends (1) and (2) discussed in text.

154x249mm (300 x 300 DPI)

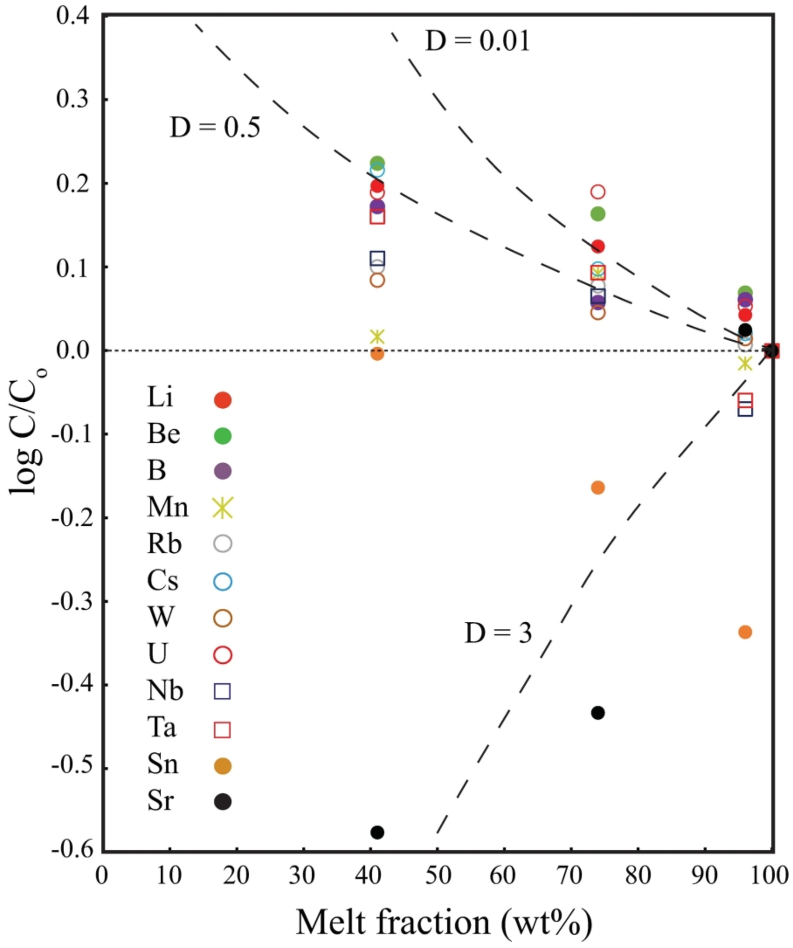

Pichavant, Fig.9

Fig. 9. Evolution of trace element concentrations during progressive crystallization of the B2 Beauvoir melt. Concentrations of trace elements (Li, Be, B, Mn, Rb, Cs, W, U, Nb, Ta, Sn, Sr) in selected B2 glasses (C), referenced to those in the initial melt (C0, represented by the crystal-free charge B2N-26), are plotted as log (C/C0) vs. the melt fraction (f). Glass concentrations are from Table 9 and melt fractions from Table 3. Dashed curves are Rayleigh fractionation trends calculated (see Hanson, 1978) for bulk mineral/melt partition coefficients (D) of 0.01, 0.5 and 3. The horizontal dotted line corresponds to C = C0. See text.

175x249mm (300 x 300 DPI)

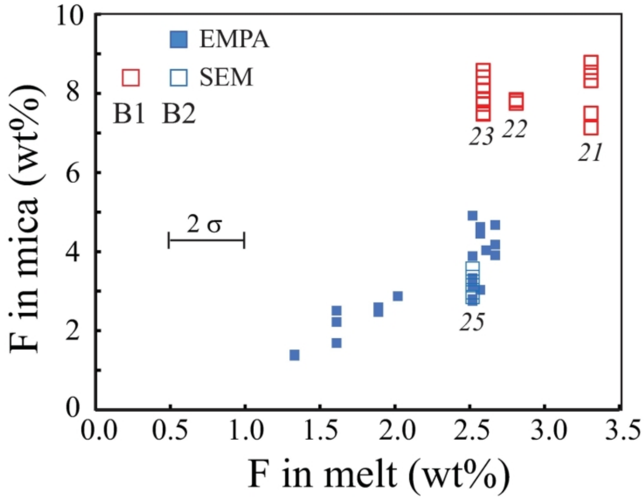

Pichavant, Fig.10

Fig. 10. F concentration in experimental micas as a function of the F content of the coexisting melt. Data for experimental micas include electron microprobe (EMPA) and SEM analyses (Table 7 and S3). F concentrations from SEM data are corrected by a constant factor (x 2.3). F concentrations in experimental melts are raw data from Table 4 (i.e., not normalized to 100%) with error bar shown. 21, 22, 23, 25 refer to the charge number in Table 2 (i.e., 21-23 refers to the B1N-21 to -23 and 25 to the B2N-25 charge).

149x224mm (300 x 300 DPI)

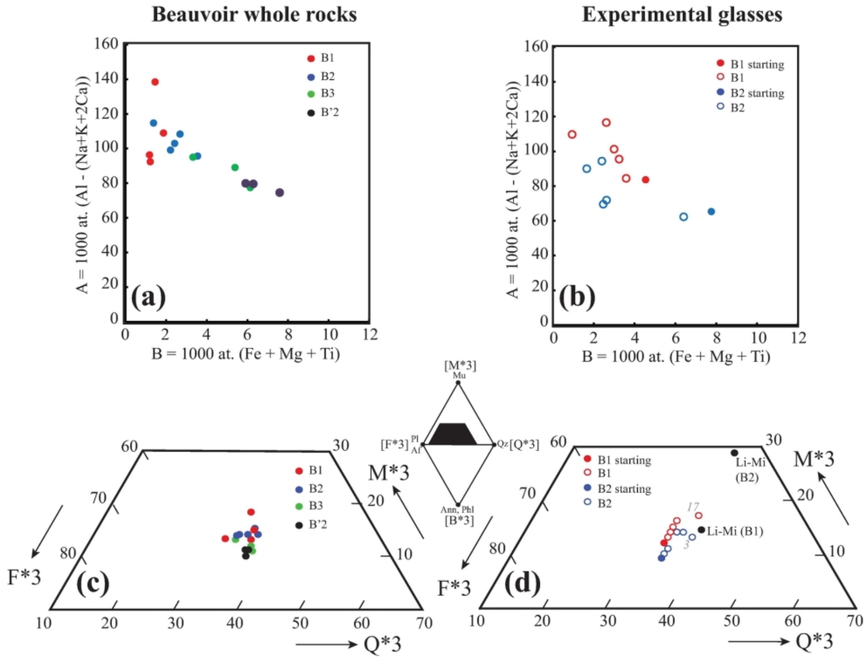

Pichavant, Fig. 11

Fig. 11. Comparison between major element fractionation in Beauvoir granites (left column) and in experimental glasses from this study (right column). Top panels (a) and (b): major element compositions plotted in the A-B diagram of Debon and Le Fort (1983). Bottom panels (c) and (d): major element compositions plotted in the Q*3-B*3-F*3-M*3 representation of La Roche et al. (1980), see also Cuney and Marignac (2015) and inset for the significance of the Q*3, B*3, F*3, M*3 apexes. Concentrations are expressed in millications, i.e., as 1000 x atomic concentrations (at.). Abbreviations: Qz: quartz, Ann: annite, Phl: phlogopite, Pl: plagioclase, Af: K-feldspar, Mu: muscovite. In (d), experimental mica compositions from charges B1N23 and B2N-25 are also plotted (respectively Li-Mi B1 and Li-Mi B2). The Beauvoir whole rock data are exclusively from Raimbault et al. (1995) and the experimental data are from this paper (averages of starting compositions in Table 1 and selected glass compositions from Table 4). Notice the specific Q*3-rich compositions of glasses B1N-17 and B2N-3 (respectively labelled 17 and 3) from 100 MPa crystallization charges.

171x221mm (300 x 300 DPI)

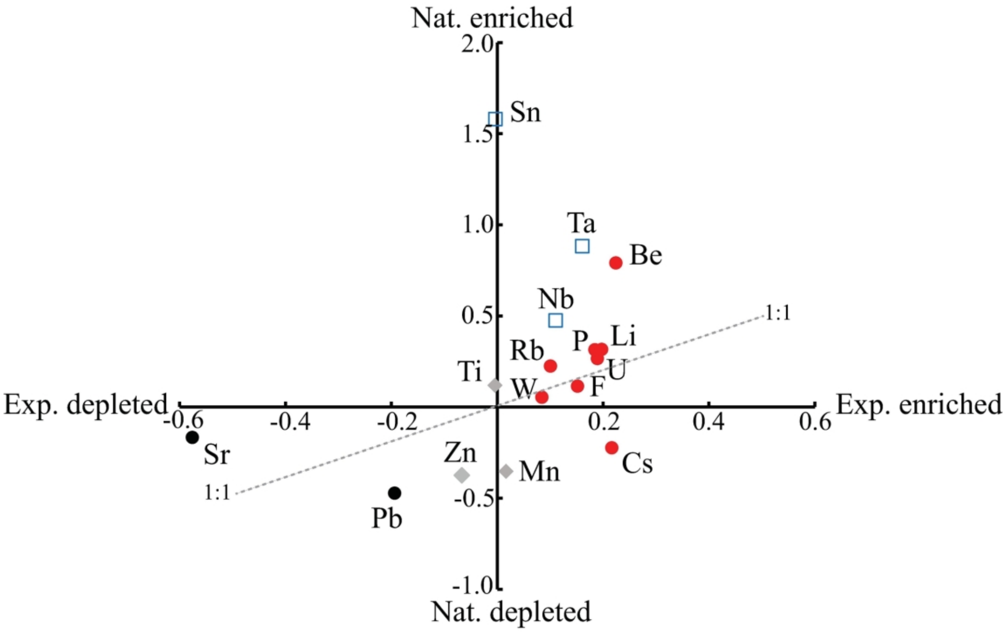

Pichavant, Fig.12

Fig. 12. Comparison between trace element (Sn, Ta, Be, Nb, Li, P, U, F, Rb, W, Ti, Mn, Zn, Pb, Sr, Cs) fractionation in experiments from this study and in Beauvoir granites. Horizontal axis: log (C/C0) where C is the trace element concentration in the most fractionated glass B2-24 and C0 the trace element concentration in the parental glass B2-26 (Table 9). Vertical axis: log (C/C0) where C is the trace element concentration in B1 granite (ESP 270, Raimbault et al., 1995) and C0 the trace element concentration in glass B2-26 (Table 9) assumed representative of the B2 granite. Experimental and natural enrichment and depletion directions are indicated. The location of data points relative to the 1:1 dotted line indicates how close elements are from an evolution identical in experiments and granites, whether an enrichment or a depletion. Color coding reflects the four groups of elements distinguished, those enriched both in the experiments and in the granites (red circles), those depleted both in the experiments and in the granites (black circles), those whose behavior should be controlled by accessory phase solubilities (blue squares) and those very much fractionated neither in the experiments nor in the granite (grey diamonds).

187x223mm (300 x 300 DPI)

Table 1. Compositions of starting materials

sample #	B1 WR	B1 glass 1997	B2 WR	B2 glass 1997	B2 glass 2017	
n		6		6	10	
		av*		av*	av	sd
SiO_2	69.04	69.36	71.62	71.18	72.47	0.88
TiO_2	0.03	0.03	0.02	0.01	0.02	0.03
Al_2O_3	16.72	16.48	15.79	15.66	14.78	0.87
Fe_2O_3	0.05	nd	0.04	nd	nd	nd
FeO	0.12	0.33	0.47	0.62	0.40	0.06
MnO	0.03	0.02	0.10	0.09	0.07	0.06
MgO	0.02	0.04	0.01	0.04	0.01	0.01
CaO	0.22	0.40	0.19	0.32	0.18	0.05
Na_2O	5.11	5.16	4.52	4.50	4.48	0.23
K_2O	3.17	2.97	3.84	3.89	4.07	0.16
P_2O_5	1.50	1.52	0.95	0.85	0.51	0.15
SnO_2	nd	nd	nd	nd	0.00	0.01
F	2.39	1.70	1.77	1.20	2.05	0.30
Li_2O	1.28	nd	0.71	nd	nd	nd
CO_2	0.03	nd	0.03	nd	nd	nd
H_2O	0.40	nd	0.23	nd	nd	nd
Total	98.83	98.01	99.58	98.36	99.04	
O=F	1.01	0.72	0.75	0.51	0.86	
Total	97.82	97.29	98.83	97.86	98.18	
Qz	28.34	28.73	31.50	30.78	31.72	
Ab	45.87	46.29	39.86	39.88	39.51	
Or	19.87	18.59	23.65	24.06	25.04	
An	1.16	2.10	0.98	1.66	0.94	
Co	4.76	4.29	4.02	3.62	2.79	
Total	100.00	100.00	100.00	100.00	100.00	
A/CNK	1.37	1.33	1.32	1.28	1.22	

Granite whole-rock (WR) samples analyzed by wet chemistry (Pichavant et al.. 1987a)

Glasses analyzed by electron microprobe. n: number of electron microprobe spots; av: average; sd: standard deviation

*data from Lahlafi (1997)

FeO = FeO total except for the WR data (FeO = FeO)

nd: not determined

Qz, Ab, Or, An, Co: normative quartz, albite, orthoclase, anorthite and corundum concentrations

A/CNK = $Al_2O_3/(Na_2O+K_2O+CaO)$ molar

Table 2. Conditions and results of the B1 crystallization experiments.

Charge #	T °C	P MPa	duration h	phase assemblage	Σr^2	fO_2 control	ΔNNO	Reference
Nancy								
B1N-16	540	100	2064	Qz, Pl, Af, Mu	nd	unbuffered	~+3	
B1N-11	560	100	1800	(L), Qz, Pl, Af, Mu	nd	unbuffered	~+3	(1)
B1N-17	580	100	2064	L(60), Qz(8), Pl(24), Af(6), Mu(1), Ap	0.03	unbuffered	~+3	
B1N-1	600	100	1800	L(84), Qz (2), Pl(13), Mu(1)	0.09	unbuffered	~+3	(1)
B1N-13	640	100	1104	L(100)	nd	unbuffered	~+3	(1)
B1N-9	660	100	1560	L(100)	nd	unbuffered	~+3	(1)
B1N-7	680	100	1560	L(100)	nd	unbuffered	~+3	(1)
B1N-2	700	100	672	L(100)	nd	unbuffered	~+3	(1)
B1N-21	580	300	2184	L(67), Qz(9), Pl(16), Af(6), Mu(1) Tpz, Li-P, Ap	0.00	unbuffered	~+3	
B1N-15	600	300	1104	L(98), Pl(2), Ap	0.11	unbuffered	~+3	(1)
B1N-22	620	300	2184	L(77), Qz(7), Pl(14), Af(2), (Mu), Ap	0.01	unbuffered	~+3	
B1N-23	640	300	2184	L(85), Qz(2), Pl(12), (Mu), Ap	0.06	unbuffered	~+3	
Orléans								
B1O-1	620	300	1008	L(98), Pl(2), Ap	0.02	intrinsic	+1	

L: silicate glass, Qz: quartz, Pl: plagioclase, Af: K-feldspar, Mu: muscovite, Tpz: topaz, Li-P: amblygonite, Ap: apatite.

ΔNNO: deviation in log fO_2 from the NNO oxygen buffer (Chou, 1987) calculated at the same P and T than the experiment.

Numbers in brackets are proportions of major phases (wt%) calculated by mass balance. Σr^2 = sum of residuals. (phase A): < 1 wt% phase A present.

(1) experiments partially described in Pichavant et al. (1987a).

Table 3. Conditions and results of the B2 crystallization experiments.

Charge #	T °C	P MPa	duration h	phase assemblage	Σr^2	fO_2 control	ΔNNO	Reference
Nancy								
B2N-12	560	100	1800	(L), Qz, Pl, Af, Mu	nd	unbuffered	~+3	(1)
B2N-3	600	100	1080	L(63), Qz(9), Pl(15), Af(9), Mu(4)	0.00	unbuffered	~+3	(1)
B2N-20	620	100	2064	L(29), Qz(20), Pl(28), Af(20), Mu(4), Hm	0.14	unbuffered	~+3	
B2N-14	640	100	1104	L(100)	nd	unbuffered	~+3	(1)
B2N-10	660	100	1560	L, Hm	nd	unbuffered	~+3	(1)
B2N-8	680	100	1560	L, Hm	nd	unbuffered	~+3	(1)
B2N-4	700	100	672	L(100)	nd	unbuffered	~+3	(1)
B2N-18	620	200	2064	L(74), Qz(10), Pl(11), Mu(5)	0.00	unbuffered	~+3	
B2N-19	640	200	2064	L(87), Qz(5), Pl(5), Mu(3), Hm	0.08	unbuffered	~+3	
B2N-24	580	300	2184	L(41), Qz(19), Pl(21), Af(10), Mu(9)	0.02	unbuffered	~+3	
B2N-25	620	300	2184	L(96), Qz(2), Mu(2), Hm, Ap	0.07	unbuffered	~+3	
B2N-26	640	300	2184	L(100)	nd	unbuffered	~+3	
Orléans								
B2O-2/5*	620	300	1008-4032	L, Qz, Pl, (Af), Mu, Mt, Ap	nd	intrinsic	+1	(2)
B2O-6/7*	700	300	168-1008	L, Ap, Mt	nd	intrinsic	+1	(2)
B2O-38/40*	620	300	240-360	L(98), Bt(2), Ap	0.49	CCO buffer	-1.4	(2)
B2O-41	700	300	168	L, Ap	nd	CCO buffer	-1.4	(2)
B2O-50	630	304	1123	L(95), Mu(5), Ap	0.15	$Ar-H_2$	-1	

L: silicate glass, Qz: quartz, Pl: plagioclase, Af: K-feldspar, Mu: muscovite, Bt: biotite, Ap: apatite, Hm, hematite, Mt: magnetite.
ΔNNO: deviation in log fO_2 from the NNO oxygen buffer (Chou, 1987) calculated at the same P and T than the experiment.
Numbers in brackets are proportions of major phases (wt%) calculated by mass balance. Σr^2 = sum of residuals. nd: not determined (mass balance calculation not performed). (phase A): < 1 wt% of phase A present.
*Multiple experiments were performed for different durations under identical P-T conditions and results are grouped (see text).

(1) experiments partially described in Pichavant et al. (1987a).
(2) experiments partially described in Lahlafi (1997) and Pichavant et al. (2016).

Table 4. Major element compositions of experimental glasses

sample #	B1		B1		B1		B1	
charge #	B1N-1		B1N-15		B1N-17		B1N-21	
n	5		5		6		6	
	av	sd	av	sd	av	sd	av	sd
SiO_2	63.37	0.22	62.70	0.63	61.56	0.55	61.90	0.98
TiO_2	0.01	0.01	0.00	0.01	0.02	0.02	0.01	0.01
Al_2O_3	15.23	0.23	15.42	0.26	15.85	0.27	16.54	0.62
FeO	0.19	0.11	0.13	0.09	0.15	0.08	0.05	0.05
MnO	0.03	0.04	0.04	0.04	0.04	0.05	0.04	0.05
MgO	0.04	0.05	0.03	0.02	0.01	0.02	0.01	0.01
CaO	0.04	0.02	0.06	0.03	0.04	0.02	0.07	0.02
Na_2O	4.40	0.11	4.73	0.11	3.95	0.20	4.67	0.19
K_2O	3.34	0.03	3.07	0.09	3.08	0.15	2.91	0.19
P_2O_5	1.51	0.16	1.42	0.14	1.70	0.18	1.38	0.09
SnO_2	nd		nd		nd		nd	
F	2.37	0.10	2.26	0.05	3.16	0.09	3.31	0.32
Total	90.52		89.87		89.55		90.88	
O=F	1.00		0.95		1.33		1.39	
Total	89.52		88.91		88.22		89.49	
Qz	28.86		27.07		31.61		27.26	
Ab	43.07		46.58		39.59		45.89	
Or	22.84		21.13		21.54		19.96	
An	0.26		0.33		0.22		0.39	
Co	4.99		4.89		7.04		6.50	
Total	100.00		100.00		100.00		100.00	
A/CNK	1.39		1.37		1.60		1.51	

Glasses analyzed by electron microprobe. n: number of electron microprobe spots; av: average; sd: standard deviation. For B1, glasses from charges B1N-11, -13, -9, -7, -2 (Table 2) have not been analyzed and for B2, glasses from charges B2N-10, -8, -4 and B2O-6/7, -41 (Table 3)

*data from Lahlafi (1997) normalized to 100%

FeO = FeO total

nd: not determined

Qz, Ab, Or, An, Co: normative quartz, albite, orthoclase, anorthite and corundum concentrations

A/CNK = $Al_2O_3/(Na_2O+K_2O+CaO)$ molar

B1		B1		B1	B2		B2	
B1N-22		B1N-23		B1O-1	B2N-3		B2N-14	
5		6		6	5		5	
av	sd	av	sd	av*	av	sd	av	
62.22	0.54	63.20	0.44	71.19	65.93	0.66	65.48	1.13
0.01	0.02	0.01	0.01	0.02	0.02	0.02	0.01	0.02
16.10	0.24	16.00	0.18	17.22	14.43	0.16	14.38	0.57
0.15	0.04	0.19	0.12	0.03	0.16	0.08	0.19	0.06
0.05	0.07	0.06	0.08	0.00	0.14	0.05	0.08	0.06
0.03	0.04	0.02	0.02	0.01	0.01	0.01	0.01	0.01
0.07	0.03	0.05	0.01	0.13	0.12	0.03	0.16	0.02
4.43	0.12	4.52	0.11	5.20	3.72	0.20	4.10	0.18
3.25	0.10	3.31	0.04	3.28	3.58	0.07	3.75	0.14
1.68	0.28	1.53	0.08	1.69	1.02	0.13	0.96	0.07
nd		nd		nd	nd		nd	
2.81	0.10	2.59	0.08	2.12	1.89	0.22	1.62	0.13
90.81		91.48		100.90	90.99		90.75	
1.18		1.09		0.89	0.80		0.68	
89.63		90.39		100.00	90.20		90.07	
27.70		27.66		28.96	34.59		30.61	
43.58		43.95		45.38	35.83		39.50	
22.32		22.48		19.97	24.09		25.25	
0.40		0.31		0.66	0.67		0.92	
6.00		5.59		5.03	4.82		3.72	
100.00		100.00		100.00	100.00		100.00	
1.47		1.44		1.40	1.41		1.29	

B2		B2		B2		B2	
B2N-18		B2N-19		B2N-20		B2N-24	
7		10		6		2	
av	sd	av	sd	av	sd	av	sd
65.02	0.23	65.09	0.38	62.90	0.56	64.50	0.46
0.02	0.02	0.03	0.05	0.03	0.02	0.02	0.02
15.05	0.09	14.41	0.13	15.01	0.13	15.63	0.24
0.30	0.13	0.12	0.03	0.08	0.05	0.14	0.13
0.07	0.03	0.07	0.07	0.12	0.07	0.07	0.08
0.01	0.01	0.02	0.02	0.01	0.01	0.01	0.01
0.13	0.03	0.18	0.02	0.15	0.03	0.04	0.02
4.31	0.11	4.03	0.17	3.96	0.20	4.38	0.25
3.99	0.04	3.61	0.14	3.36	0.23	3.27	0.12
1.11	0.10	1.01	0.17	1.27	0.14	1.27	0.13
nd		0.00		nd			
2.02	0.15	2.67	0.33	2.57	0.07	2.61	0.09
92.04		91.24		89.45		91.94	
0.85		1.12		1.08		1.10	
91.19		90.11		88.37		90.84	
27.55		31.45		31.25		30.07	
41.19		39.03		39.24		42.25	
26.66		24.43		23.28		22.00	
0.75		1.03		0.86		0.21	
3.84		4.06		5.38		5.48	
100.00		100.00		100.00		100.00	
1.29		1.33		1.44		1.44	

B2		B2		B2	B2	B2	
B2N-25		B2N-26		B2O-2/5	B2O-38/40	B2O-50	
2		10		8	12	6	
av	sd	av	sd	av*	av*	av	sd
64.80	0.56	64.52	0.39	73.48	73.97	67.79	0.66
0.01	0.02	0.03	0.05	0.02	0.04	0.02	0.03
14.46	0.23	13.94	0.21	15.76	15.79	13.72	0.21
0.16	0.03	0.42	0.05	0.16	0.51	0.36	0.05
0.08	0.06	0.09	0.07	0.11	0.09	0.07	0.07
0.01	0.01	0.01	0.01	0.07	0.03	0.01	0.01
0.08	0.05	0.15	0.02	0.11	0.27	0.16	0.04
4.13	0.14	3.99	0.15	4.57	4.07	4.38	0.20
3.55	0.10	3.63	0.17	3.77	3.78	3.66	0.12
0.85	0.39	1.00	0.12	1.19	0.74	0.41	0.10
0.01	0.01	0.01	0.01	nd	nd	0.00	0.01
2.52	0.31	2.33	0.32	1.33	1.24	1.61	0.32
90.65		90.11		100.57	100.53	92.19	
1.06		0.98		0.56	0.52	0.68	
89.59		89.12		100.01	100.01	91.51	
31.02		31.43		32.96	36.01	31.15	
40.20		39.17		39.61	35.18	41.35	
24.10		24.87		22.82	22.85	24.07	
0.46		0.85		0.55	1.35	0.91	
4.22		3.68		4.05	4.61	2.52	
100.00		100.00		100.00	100.00	100.00	
1.34		1.30		1.34	1.40	1.20	

Table 5. Representative compositions of experimental quartz

sample #	B1		B1	B1	B1	B2	B2	B2	B2
charge #	B1N-17		B1N-21	B1N-22	B1N-23	B2N-3	B2N-18	B2N-19	B2N-20
SiO_2	94.59	94.12	98.67	98.49	99.78	98.52	99.15	99.89	99.25
TiO_2	0.00	0.00	0.04	0.00	0.00	0.00	0.00	0.00	0.03
Al_2O_3	2.88	3.01	0.43	0.08	0.18	0.20	0.08	0.23	0.33
FeO	0.00	0.00	0.01	0.07	0.00	0.00	0.00	0.01	0.13
MnO	0.07	0.06	0.08	0.06	0.00	0.00	0.13	0.00	0.00
MgO	0.00	0.01	0.00	0.00	0.00	0.00	0.00	0.00	0.01
CaO	0.00	0.00	0.00	0.00	0.02	0.01	0.03	0.01	0.00
Na_2O	0.02	0.11	0.05	0.00	0.02	0.01	0.01	0.03	0.00
K_2O	0.00	0.09	0.01	0.01	0.02	0.00	0.00	0.00	0.06
P_2O_5	0.09	0.14	0.03	0.00	0.00	0.00	0.05	0.09	0.05
SnO2	nd	nd	nd	nd	nd	nd	nd	nd	nd
F	0.00	0.00	0.00	0.00	0.00	0.00	0.00	0.00	0.00
Total	97.66	97.53	99.31	98.71	100.01	98.74	99.44	100.25	99.87
O=F	0.00	0.00	0.00	0.00	0.00	0.00	0.00	0.00	0.00
Total	97.66	97.53	99.31	98.71	100.01	98.74	99.44	100.25	99.87

FeO = FeO total

nd: not determined

Table 6. Representative compositions of experimental feldspars

sample #	B1		B1	B1			B1		B1	
charge #	B1N-1		B1N-15	B1N-17			B1N-21		B1N-22	
feldspar	Pl	Pl*	Pl*	Pl	I	Af	Pl	Af	Pl	Af
SiO_2	65.12	67.87	67.41	67.15	65.09	64.22	67.43	63.93	66.90	63.31
TiO_2	0.02	nd	nd	0.02	0.00	0.00	0.00	0.00	0.00	0.00
Al_2O_3	19.75	20.31	20.13	19.47	19.34	19.78	20.46	19.06	20.43	19.09
FeO	0.00	nd	nd	0.00	0.12	0.00	0.00	0.00	0.07	0.19
MnO	0.22	nd	nd	0.00	0.00	0.07	0.06	0.00	0.00	0.00
MgO	0.00	nd	nd	0.00	0.00	0.00	0.00	0.00	0.01	0.00
CaO	0.57	0.18	0.15	0.12	0.35	0.03	0.51	0.01	0.53	0.00
Na_2O	10.06	10.30	10.27	9.39	6.81	3.41	9.99	2.91	9.83	3.26
K_2O	1.40	1.24	1.23	2.00	5.80	11.55	1.62	12.28	1.50	11.62
P_2O_5	1.36	nd	nd	1.24	1.25	0.96	0.66	1.02	1.15	0.82
F	0.00	nd	nd	0.00	0.25	0.01	0.04	0.10	0.09	0.00
Total	98.48	99.90	99.19	99.39	99.00	100.02	100.77	99.30	100.51	98.29
O=F	0.00	0.00	0.00	0.00	0.10	0.00	0.02	0.04	0.04	0.00
Total	98.48	99.90	99.19	99.39	98.89	100.02	100.75	99.26	100.47	98.29
Or	8.1	7.3	7.3	12.2	35.3	68.9	9.4	73.5	8.9	70.1
Ab	89.1	91.8	92.0	87.2	62.9	30.9	88.1	26.5	88.5	29.9
An	2.8	0.9	0.7	0.6	1.8	0.2	2.5	0.0	2.7	0.0

Pl: plagioclase; Af: K-feldspar, I: heterogeneous feldspar

*data from Pichavant et al. (1987a)

**data from Lahlafi (1997)

FeO = FeO total

nd: not determined

Ab, Or, An: molar proportions of albite, orthoclase, anorthite end-members

B1	B1	B2					B2	B2	B2	
B1N-23	B1O-1	B2N-3					B2N-18	B2N-19	B2N-20	
Pl	Pl**	Pl	Pl*	Af	I	Af*	Pl	Pl	Pl	I
66.90	65.75	66.23	66.50	64.47	63.36	65.29	66.20	66.06	65.82	64.55
0.00	nd	0.00	nd	0.00	0.00	nd	0.00	0.03	0.00	0.01
20.43	20.04	20.72	20.48	19.05	19.49	19.48	20.31	20.57	20.94	20.15
0.07	nd	0.17	nd	0.28	0.00	nd	0.06	0.11	0.14	0.00
0.00	nd	0.13	nd	0.00	0.00	nd	0.00	0.15	0.00	0.03
0.01	nd	0.00	nd	0.01	0.03	nd	0.01	0.01	0.00	0.00
0.53	0.43	0.57	0.69	0.00	0.13	0.01	0.60	0.88	0.80	0.41
9.83	10.55	10.45	9.19	4.54	5.61	4.90	10.08	10.44	9.60	8.57
1.50	0.94	1.17	2.25	9.88	8.74	9.04	1.67	1.02	1.55	4.34
1.15	0.90	1.04	nd	1.01	0.67	nd	0.84	0.91	0.88	1.08
0.09	nd	0.00	nd	0.00	0.00	nd	0.00	0.00	0.05	0.00
100.51	98.61	100.48	99.11	99.23	98.03	98.72	99.77	100.18	99.78	99.14
0.04	0.00	0.00	0.00	0.00	0.00	0.00	0.00	0.00	0.02	0.00
100.47	98.61	100.48	99.11	99.23	98.03	98.72	99.77	100.18	99.76	99.14
8.9	5.4	6.7	13.4	58.9	50.3	54.8	9.6	5.8	9.2	24.5
88.5	92.5	90.6	83.2	41.1	49.1	45.1	87.6	90.0	86.8	73.5
2.7	2.1	2.7	3.5	0.0	0.6	0.1	2.9	4.2	4.0	2.0

	B2		B2
	B2N-24		B2O-2/5
Af	Pl	Af	I**
63.78	66.77	66.28	63.45
0.00	0.01	nd	nd
19.04	20.16	19.91	18.49
0.00	0.00	nd	nd
0.00	0.00	nd	nd
0.00	0.01	nd	nd
0.07	0.17	0.2	0.07
4.52	10.25	7.52	2.89
10.03	1.75	5.23	11.60
0.92	0.75	0.9	0.44
0.06	0.00	nd	nd
98.43	99.88	100.04	96.94
0.02	0.00	0.00	0.00
98.40	99.88	100.04	96.94
59.1	10.0	31.1	72.3
40.5	89.2	67.9	27.4
0.3	0.8	1.0	0.4

Table 7. Representative compositions of experimental micas

sample #	B1	B1	B1	B2	B2	B2	B2	B2	B2	B2	B2
charge #	B1N-21	B1N-22	B1N-23	B2N-3	B2N-18	B2N-19	B2N-20	B2N-24	B2N-25	B2O-2/5*	B2O-50
SiO_2	53.61	51.19	51.04	47.36	45.92	45.00	45.62	47.07	43.70	45.00	45.74
TiO_2	nd	nd	nd	0.21	0.20	0.05	0.00	0.00	0.00	0.04	0.06
Al_2O_3	21.50	19.74	20.01	29.56	31.88	34.25	34.90	30.25	32.82	33.25	33.66
FeO	2.18	5.34	5.40	7.43	5.12	2.87	1.81	4.57	4.92	3.49	2.28
MnO	nd	nd	nd	0.17	0.17	0.07	0.22	0.44	0.00	0.04	0.00
MgO	0.16	1.17	2.26	0.60	0.47	0.27	0.11	0.10	0.16	0.29	0.26
CaO	nd	nd	nd	0.02	0.04	0.02	0.00	0.03	0.05	0.00	0.00
Li_2O	6.75	6.04	6.80	1.31	1.75	2.62	3.00	2.50	1.79	0.61	1.13
Na_2O	2.03	1.30	1.43	0.83	0.70	1.02	1.26	0.87	0.85	0.85	0.95
K_2O	6.24	7.26	7.12	9.17	10.15	8.96	9.56	9.13	9.65	9.59	10.12
P_2O_5	0.78	0.78	0.23	0.17	0.10	0.39	0.30	0.23	0.06	0.00	0.24
SnO_2	nd	nd	nd	nd	nd	0.17	0.11	0.10	0.14	nd	0.03
F	8.53	7.84	8.58	2.47	2.87	4.18	4.62	4.03	3.14	1.40	2.22
Total	101.79	100.66	102.87	99.31	99.37	99.89	101.51	99.33	97.27	94.56	96.69
O=F	3.59	3.30	3.61	1.04	1.21	1.76	1.95	1.70	1.32	0.59	0.94
Total	98.19	97.36	99.26	98.27	98.16	98.13	99.57	97.63	95.95	93.98	95.76
Mg-Li	-3.2555	-2.8253	-2.9487	-0.5697	-0.8262	-1.2878	-1.4836	-1.2776	-0.9247	-0.2760	-0.5502
Fe_t+Mn+Ti-Al^{VI}	-1.3250	-0.7700	-0.6168	-1.9034	-2.2680	-2.5341	-2.6212	-2.1248	-2.3983	-2.9863	-2.9897

Analyses by SEM for the B1 and by EMPA for the B2 charges

Li_2O estimated from the F concentration (Tischendorf et al., 1997)

*data from Lahlafi (1997)

FeO = FeO total

Table 8. Representative compositions of accessory phases

sample #	B1				B2			
charge #	B1N-21				B2N-25	B2N-19		B2N-25
phase	topaz	topaz	amblygonite	amblygonite	apatite	hematite	hematite	hematite
SiO_2	32.07	37.01	4.56	2.05	0.07	1.26	0.95	0.13
TiO_2	0.03	0.00	0.19	0.11	0.08	0.14	0.33	2.42
Al_2O_3	57.60	50.47	35.34	35.39	0.01	2.71	2.22	0.79
FeO	0.04	0.04	0.11	0.03	0.32	83.14	85.19	83.53
MnO	0.15	0.07	0.14	0.00	3.63	0.13	0.23	0.00
MgO	0.04	0.01	0.02	0.04	0.03	0.00	0.04	0.02
CaO	0.02	0.05	0.00	0.03	51.84	0.00	0.05	0.02
Na_2O	0.06	0.49	0.24	0.23	0.00	0.13	0.11	0.00
K_2O	0.08	0.30	0.39	0.05	0.00	0.12	0.09	0.00
P_2O_5	0.98	0.78	49.57	51.69	38.15	0.11	0.00	0.00
SnO_2	0.00	0.00	0.00	0.00	0.02	1.39	1.40	1.57
F	20.93	18.33	13.25	13.07	5.63	0.22	0.13	0.00
Total	112.00	107.55	103.81	102.70	99.76	89.35	90.74	88.48
O=F	8.81	7.72	5.58	5.50	2.37	0.09	0.06	0.00
Total	103.18	99.83	98.23	97.19	97.39	89.26	90.69	88.48
XF	0.99	0.89	0.95	0.94	1.55	Hm=0.997	0.993	0.950
XOH	0.01	0.11	0.05	0.06	-0.55	Ilm=0.003	0.007	0.050

Total Fe as FeO

XF = at. F/(F+OH) with F+OH = 2 for topaz and apatite and F+OH = 1 for amblygonite

XOH = 1-XF

Hm=hematite, Ilm=ilmenite

Table 9. Selected trace element concentrations

sample #	B2								B2	B2
charge #	B2N-26		B2N-25		B2N-18		B2N-24		B2N-25	B2N-25
phase	Glass		Glass		Glass		Glass		Quartz	Kd Qz/L
	av (ppm)	sd/av(%)	av (ppm)	sd/av(%)	av (ppm)	sd/av(%)	av (ppm)	sd/av(%)	ppm	
Li	2737.6	1.1	3021.1	3.8	3648.6	5.2	4310.3	10.8	81.3	0.027
Be	32.0	3.3	37.5	7.8	46.6	8.6	53.6	15.8	<0.8	
B	10.0	4.9	11.6	9.3	11.5	10.6	14.9	19.2	<1.9	
Na	26154.3	1.5	27739.9	1.7	27848.6	3.9	29257.3	6.9	<22.6	
Al	66231.2	2.0	70296.0	4.8	78139.7	7.4	74862.6	5.0	367.9	0.005
P	3057.8	2.9	3110.0	3.7	3547.7	4.7	3621.3	10.3	152.8	0.049
Ti	41.8	7.5	19.4	10.5	66.9	14.5	41.4	2.2	2.4	0.123
Mn	483.0	2.0	466.4	1.4	598.8	4.4	501.8	5.0	<3.9	
Zn	114.6	6.8	108.1	4.4	110.9	9.1	98.2	8.4	2.8	0.026
Rb	2024.2	0.6	2057.8	2.9	2420.9	4.5	2550.3	7.1	<1.0	
Sr	9.0	4.7	9.5	3.5	3.3	17.9	2.4	2.7	<0.1	
Zr	3.3	6.9	2.8	26.7	4.0	12.8	4.3	7.6	<0.0	
Nb	38.1	4.0	32.5	2.3	44.3	7.0	49.2	3.6	<0.0	
Sn	35.4	3.6	16.3	26.6	24.3	16.8	35.1	22.3	3.0	0.185
Cs	624.6	1.3	655.1	2.7	782.7	4.3	1027.6	10.1	2.0	0.003
Ba	0.8	14.9	0.7	32.7	0.4	60.7	1.3	70.7	0.2	
La	0.1	13.9	0.1	72.8	0.3	21.1	0.0	6.1	<0.0	
Ta	23.2	5.7	20.2	12.2	28.7	17.6	33.5	9.3	<0.0	
W	36.2	3.6	37.4	3.6	40.2	6.2	44.0	13.5	0.1	0.002
Pb	78.1	1.6	94.8	3.4	240.5	3.5	50.0	7.8	<0.3	
U	8.6	4.5	9.7	4.2	13.3	8.6	13.3	11.4	<0.0	
Nb/Ta	1.64		1.61		1.54		1.47			

sd : standard deviation ; av : average